# Modelling Inductively Coupled Coils for Wireless Implantable Bio-Sensors, A Novel Approach Using the Finite Element Method

by

Tyler Trezise
B.Sc.E, Queen's University, 2006

A Thesis Submitted in Partial Fulfillment
of the Requirements for the Degree of

MASTER OF APPLIED SCIENCE

in the Department of Mechanical Engineering

# Supervisory Committee

Modelling Inductively Coupled Coils for Wireless Implantable Bio-Sensors,
A Novel Approach Using the Finite Element Method

by

Tyler Trezise
B.Sc.E., Queen's University, 2006

**Supervisory Committee**

Dr. Nikolai Dechev, (Department of Mechanical Engineering)
**Supervisor**

Dr. Afzal Suleman, (Department of Mechanical Engineering)
**Departmental Member**

# Abstract

**Supervisory Committee**

Dr. Nikolai Dechev, (Department of Mechanical Engineering)
**Supervisor**

Dr. Afzal Suleman, (Department of Mechanical Engineering)
**Departmental Member**

After nearly a decade of development, human-implantable sensors for detection of muscle activity have recently been demonstrated in the literature. These sensors are intended to provide better and more numerous control sources for a new generation of prosthetic devices that operate in a more natural fashion by using multiple joints and many degrees of freedom. The implantable sensors are powered and communicate wirelessly through the skin using coupled inductor coils.

The focus of the present work has been the development of a new approach to modeling the inductively coupled link by using the finite element method (FEM) to simulate a three-dimensional representation of the coils and surrounding magnetic field. This approach is attractive because it is able to encompass many physical geometric and magnetic parameters which have been a challenge to evaluate in the past.

The validity of the simulation is tested by comparison to analytically-developed formulas for self-inductance, ac resistance and mutual inductance of the coils. Determination of these parameters is necessary for calculation of the coupling coefficient between the coils, and to fully define the lumped circuit model of the link.

Use of FEM allows for more accurate simulation of configurations and materials not possible with the use of analytical formulas. For example, the complex permeability of a ferrite core is easily incorporated into the FEM model allowing for its effects to be included in the system design process. Furthermore, the three-dimensional nature of the simulation enables the calculation of transferred power for arbitrary orientations and positions of the secondary implant coil with respect to the primary coil.

Consequently, the proposed FEM approach can be a useful design tool for development of the next generation of implantable bio-sensors.

# Table of Contents

# List of Tables

# List of Figures

# List of Acronyms and Initialisms

| | |
|---|---|
| AP | action potential |
| ac | alternating current |
| AWG | American wire guage |
| DOF | degree(s)-of-freedom |
| DUT | device under test |
| dc | direct current |
| EMG | electromyogram |
| FEM | finite element method |
| FDTD | finite-difference time-domain |
| ISM | industrial scientific medical |
| IEEE | Institute of Electrical and Electronics Engineers |
| ICNIRP | International Commission on Non-Ionizing Radiation Protection |
| LAN | local area network(s) |
| MU | motor unit |
| RF | radio frequency |
| RFID | radio frequency identification |
| SAR | specific absorption rate |
| 3D | three-dimensional |
| 2D | two-dimensional |
| VNA | vector network analyzer |

# List of Symbols

| | | |
|---|---|---|
| $\alpha$ | angle between primary and secondary coil axes | |
| $C_2$ | capacitor used for resonance | F |
| $I$ | coil current | A |
| $\mathbf{J}$ | conduction current | A |
| $\sigma$ | conductivity | $S \cdot m^{-1}$ |
| $\mathbf{E_c}$ | conservative electric field component | $V\ m^{-1}$ |
| $A_k$ | correction factor | |
| $k$ | coupling coefficient | |
| $A$ | cross-sectional area | $m^2$ |
| $r$, $\varphi$, $z$ | cylindrical coordinate system coordinates | |
| $d$ | distance between coil centres | m |
| $\mathbf{D}$ | electric displacement field | $C\ m^{-2}$ |
| $\varepsilon$ | electric permittivity | $F\ m^{-1}$ |
| $\varepsilon_r$ | relative permittivity | |
| $\varepsilon_0$ | vacuum permittivity, $8.854\ldots \times 10^{-12}$ | $F\ m^{-1}$ |
| $V_1$ | electric potential across primary | V |
| $Z_{eq}$ | equivalent impedance | Ω |
| $R'$ | equivalent series resistance | Ω |
| $\mathbf{J^e}$ | external source current density | $A\ m^{-2}$ |
| $K(m)$ $E(m)$ | first and second kind of elliptic integrals | |
| $\Lambda$ | flux linkage | |
| $f$ , $\omega$ | frequency | Hz, rad |
| $L'$ | frequency-dependent self-inductance | H |
| $\Delta\omega$ | half-power (3dB) bandwidth | |
| $\theta$ | impedance phase angle | |
| $R_L$ | load resistor representing implant circuit | Ω |
| $\mathbf{H}$ | magnetic field | $A\ m^{-1}$ |
| $\Phi$ | magnetic flux | Wb |
| $\mathbf{B}$ | magnetic flux density | T |
| $\mu$ | magnetic permeability | $H \cdot m^{-1}$ |
| $\mu_r$ | relative permeability | |
| $\mu_0$ | permeability of free space, $4\pi\times10^{-7}$ | $H\ m^{-1}$ |
| $\mathbf{A}$ | magnetic vector potential | $V\ s \cdot m^{-1}$ |
| $M$ | mutual inductance | H |
| $\mathbf{E_m}$ | non-conservative electric field component | $V\ m^{-1}$ |
| $N$ | number of turns | |
| $R_{1,2}$ | primary and secondary coil equivalent series resistance | Ω |
| $n_{1,2}$ | primary and secondary number of turns | |
| $L_1$ | primary coil (external) self-inductance | H |
| $Q$ | quality factor | |
| $\rho$ | resistivity | $\Omega \cdot m$ |
| $\omega_0$ | resonant frequency | rad |
| $L_2$ | secondary coil (implant) self-inductance | H |
| $L$ | self-inductance | H |
| $\delta$ | skin depth | m |
| $h$, $l$ | solenoid length | m |
| $r$ | solenoid radius | m |
| $C_{TOT}$ | total secondary parallel capacitance | F |
| $\nabla$ | vector differential operator | |
| $\lambda$ | wavelength | m |

# Acknowledgments

I would like to thank Dr. Dechev for his guidance, for supporting the work, and for his valuable comments towards the preparation of this document

Thanks to my parents Janet and John for their encouragement and to Carley for her support.

# 1 Introduction

The state-of-the-art in conventional electric hand and arm prosthesis technology is currently limited. Although there are many advanced electromechanical prosthesis designs in development, the technology enabling intuitive control of these advanced multi-channel (multiple degree-of-freedom) prostheses has yet to be fully realized. Hence most existing upper limb prostheses are operated with a single channel, allowing a gripper to open and close, or a wrist joint to rotate. Advanced prosthesis designs promise natural arm movements with the controlled articulation of mechanical fingers, but they have remained at the research stage because their high level of mobility cannot be controlled with present methods. These lifelike devices require a more sophisticated control scheme that uses a forward dynamics model requiring many individual muscle activations as input.

In conventional myoelectric prosthesis control, electrodes on the skin of the residual limb detect underlying muscle activations as electric potentials. Their combination produces an electromyogram (EMG), which is the superposition of activation potentials from many muscles. To isolate the activations, various algorithms have been developed, but ideally more selective detection is needed. More precisely targeted measurement may be obtained by using needle electrodes; but a transcutaneous connection (through the skin) is not feasible for application to prostheses. Therefore, implantable EMG sensors have been proposed, since they can provide the selective (localized) EMG measurement that is desired.

In order to power implantable sensors, and yet have them operate for years, batteries are not feasible. Hence, there is much interest in powering implantable devices wirelessly. Over the last decade researchers have made progress in this direction, recently reporting some preliminary results [1].

The focus of this thesis is the development of a computational modelling method to facilitate the design of implantable sensors. Specifically, the electromagnetic link that inductively couples an implanted sensor to the outside world has been examined.

Many existing implantable medical devices have been developed that receive power [2-4], and report collected data [5-8] wirelessly. The wireless electromagnetic connection is achieved through inductive coupling of coiled conductors. In particular, solenoid shaped (helical) coils are investigated due to their geometrical fit to the problem. In the proposed application of this work, the power transmitting coil is incorporated into the prosthesis socket worn on the residual upper limb. The receiving coil is incorporated with the implanted sensor, and is then located within the volume enclosed by the transmitting coil. This configuration is envisioned as illustrated in Figure 1.1.

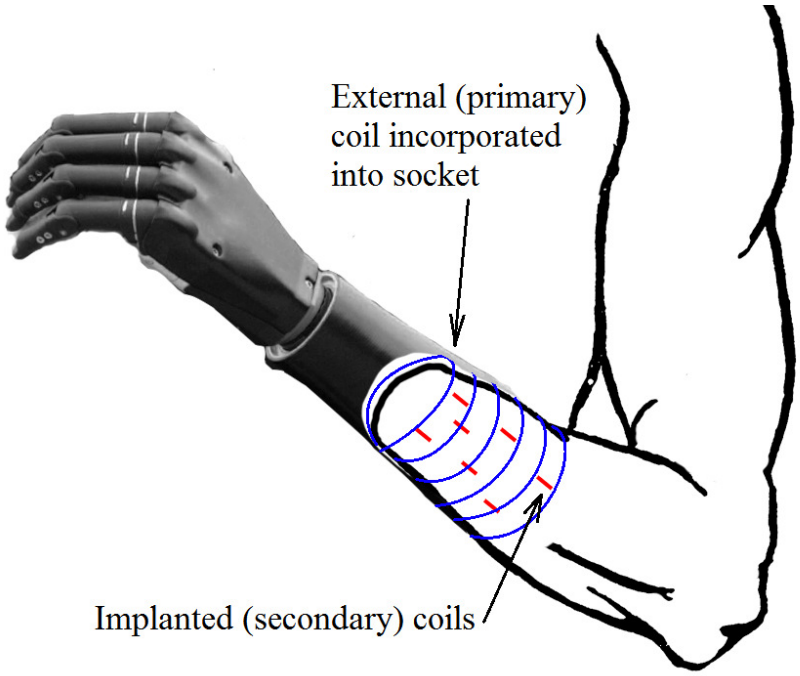


**Figure 1.1 Configuration of primary and secondary (implant) coils**

Created sufficiently small, a sensor could be implanted into each muscle of the residual limb, enabling the direct measurement of a highly localized EMG, as required for the forward dynamics control strategy proposed above. Minimizing the size of the implanted device also reduces the invasive nature of a foreign object to the body.

An initial design concern is the availability of power for the implanted EMG sensor circuit. There are numerous variables in the calculation that dictates the available power. These have traditionally been approximated by analytically developed formulas. Additionally, prototype coils may be constructed and measured as a more laborious method to quantify these variables and hence calculate the power transferred wirelessly.

Many of the variables are affected by the geometry of the coupled coils. For instance, the inductance of each coil is determined by its number of turns, length, and diameter, as

these quantities determine the strength and spatial distribution of the surrounding magnetic field. Further, the relative position and orientation between a transmitting and receiving coil will determine how well they are magnetically coupled. If the receiving coil is not centred coaxially with the transmitter, the problem cannot be simplified by symmetry. Consequently a full three-dimensional (3D) model is proposed in the present study in order to evaluate the degree of coupling for a variety of more realistic receiver positions.

A tool frequently used for spatially-defined problems is the finite element method (FEM), where a problem is broken down into solvable pieces through discretization of its physical domain. Using this method for modelling the electromagnetic inductive coupling between coils could be a useful design tool for development of wireless sensors because it can accommodate non-symmetrical coil positions. Two-dimensional FEM has been employed to model individual inductors [9], but a 3D model of coupled coils has to date only been suggested [10]. Therefore, the present work seeks to investigate 3D FEM as a novel approach to analysis of inductively coupled coils.

An FEM approach allows a model of coupled coils to be driven by the geometry and material properties instead of loosely approximated by analytical formulas. Now the magnetic flux linking the coils may be determined quickly, while the coil parameters may be easily varied. These include the diameters, number of turns, and core materials, as well as their relative position and orientation.

To illustrate the geometry of interest, and one quantity available from the FEM solution, Figure 1.2 shows the direction and intensity of the magnetic field surrounding a coil sized to represent the externally-located coil that generates the magnetic field. In this

example there is a large field density in the centre due to the presence of high permeability magnetic material there (blue region).

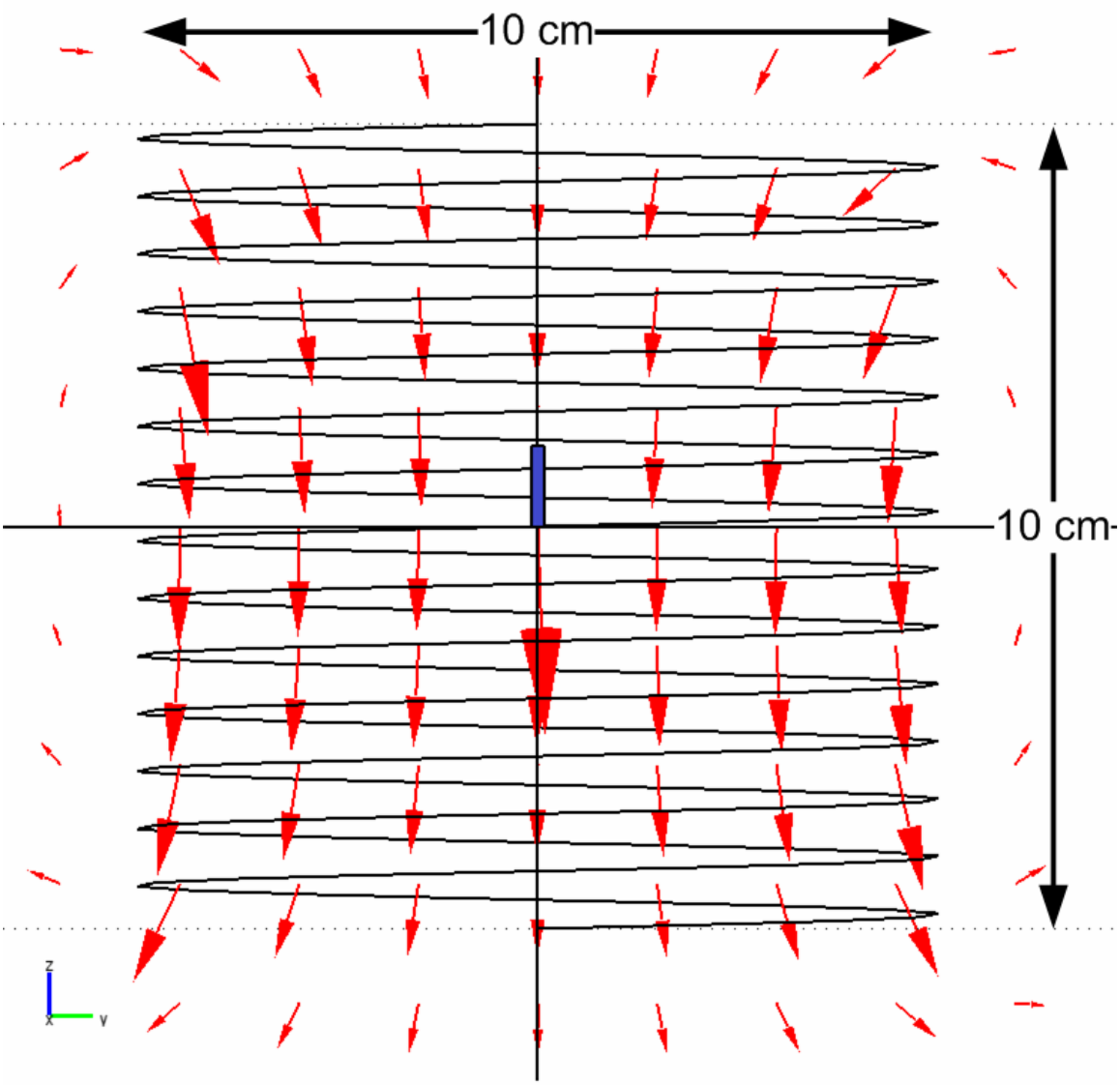


**Figure 1.2 Side view of solenoid coil with direction and magnitude of magnetic flux density (indicated by arrow size). Volume of magnetic material (blue) located centrally.**

## 1.1 Document Outline

Chapter 1 provides a further introduction to the problem and insight regarding the motivation for the work presented herein. The motivation is elaborated in chapter 2 by providing a summary of applicable background information with reference to the relevant literature. The problem of modern prosthesis control is defined here.

Initial concerns about the feasibility of an implantable device are considered in chapter 3. Here, the physical effect of an implant and electromagnetic exposure on the body is discussed, leading to the selection of the operating frequency for a wireless power link.

Chapter 4 describes the lumped circuit model of inductive wireless power transfer, as well as experimental and analytical methods towards determination of the circuit parameters.

The criteria that are desired for the proposed FEM model are listed in chapter 5. The bounds of the model are also established here.

Chapter 6 describes how the finite element method has been applied to modelling solenoid coils in two dimensions as well as their degree of coupling in three dimensions.

Chapter 7 describes the experimental set-up used to verify the simulation results.

Chapter 8 presents the results of the computation described in chapter 6, and the measurements of chapter 7, while chapter 9 consists of remarks summarizing the contributions of this work, future work, and conclusions.

# 2 Motivation and Background

## 2.1 Statement of the Problem

There are several types of commercially available prosthetic devices for people with upper limb deficiencies. These devices include passive prostheses, body-powered prostheses, and electrically-powered prostheses [11]. Most of the passive and body-powered upper limb prostheses remain largely similar to those introduced a century ago. Electric prosthesis designs attempt to combine functionality, cosmetic appearance, and an electric power source to create a useful and natural looking artificial hand. However, a majority of the commercially-available designs are only capable of opening and closing a claw-like gripper with a single degree-of-freedom (DOF) action.

To overcome this limited operation, many advanced prosthesis designs that mimic the human arm in form and function are under development [12-14], but they remain only laboratory successes because their complex actions can not be controlled intuitively by the amputee. The necessary control schemes have been developed, based on anatomically-correct musculoskeletal models, but they lack sufficient inputs. To drive these models to a desired position, the activations of the individual muscles are needed.

To some degree, these activations can be isolated from signals detected on the skin surface above the muscles. However it is difficult to achieve a consistent and repeatable placement of the sensors for this method. Variation in skin impedance and crosstalk from other muscles also prevent effective isolation of the signals.

An implantable sensor potentially offers a robust solution to the aforementioned problems. By being powered wirelessly, an implantable sensor eliminates the problems caused by a wired connection through the skin, such as tissue damage and infection, while enabling a localized and consistent measurement of muscle activity.

However, determination of the amount of power that can be transferred wirelessly to a sensor is not simple because many physical factors contribute to the calculation. These include the geometry of the coiled inductors that are coupled through a magnetic field, as well as their relative position and orientation that determine the degree to which they are coupled. Analytically-derived formulas are shown to be insufficient for determination of lumped circuit parameters, while prototyping is laborious, so it should be used to verify designs rather than initiate them.

In conclusion, the problem faced in the development of modern prostheses is the lack of intuitive control available to the user. An advanced control scheme could rectify this, but it requires many channels of simultaneous input, specifically individual muscle activation signals. Existing methods for acquisition of these signals are inadequate because they do not provide sufficiently focal detection, or are not applicable to the prosthesis application.

## 2.2 Motivation

The motivation of the present work is to develop tools and methods that will facilitate modern prosthesis development. Specifically, the development of a computational modelling approach that simulates the power transferred wirelessly to implantable EMG sensors has been the goal here. The model should account for the multitude of design parameters and variables, while providing a straightforward and relatively rapid solution for the desired unknowns.

## 2.3 Modern Prosthesis Control Challenge

Based on results from a number of surveys, the comfort and functionality of prostheses are among the chief factors affecting their rate of use by amputees [11], [15], [16]. In order to increase their functionality, recent advanced upper limb prostheses have been designed using multiple finger, thumb, and wrist joints for more lifelike operation. Each joint that can be moved independently of the others can be considered as a single degree of freedom (DOF). It is generally considered that the human arm has 7 DOF, and the human hand has 18 DOF [17]. In contrast, the best commercially available prostheses have 3 DOF or fewer [18], with a majority having only one (open and close). There are numerous research-grade devices having multiple mechanical DOF that are able to nearly reproduce the dexterity of the human arm [19-25]; however, it remains impossible to acquire focal multi-channel user input that could allow smooth and intuitive control of these advanced devices.

The more advanced prostheses on the market that do feature multiple DOF typically allow for control of only one DOF at a time, by some method of locking out the others or

through sequential selection of the active DOF [26]. Besides being slow and non-intuitive, this strategy is only feasible for a small number of DOF.

To create natural motions with multi-DOF devices, simultaneous and independent control of their joints becomes necessary. Such a control system would be most intuitive for an amputee if it could use the same biological input signals that normally initiate muscle and finger movement. These biological signals serve as the communication between the brain and the limbs. In the case where limbs are missing, amputated, or injured, the signals are still transmitted even though they are not being used, as long as the muscle tissue is still healthy.

When these input signals from the nervous system reach the muscle fibres, electric potentials are generated by the muscle cells. The electromyogram is the superposition of these potentials that can be detected inside the muscle or above it on the surface of the skin. It has been proposed that implantable sensors can be used to detect the EMG inside the muscle [1], [27-29]. By using multiple implantable sensors, one within each of the major muscles responsible for the desired motion, the intention to flex or extend can be detected and directed to the prosthesis controller for an appropriate action.

## 2.4 The Electromyogram (EMG)

Activation signals originating in the brain reach skeletal muscles by way of the spinal cord, which contains motoneuron cells. The motoneuron connects to the muscle fibres and innervates them. These are collectively known as a motor unit (MU) [30].

Living cells maintain an electric potential difference across their membrane that varies with numerous physicochemical quantities [31]. Certain types of cells are electrically

excitable, muscle and nerve cells are of this type. In these cells, a sufficient current crossing the membrane results in a change in the membrane potential called an action potential (AP). (An insufficient current results in a smaller graded potential).

More specifically, when a nerve impulse reaches a muscle fibre, the membrane is depolarized (potential difference is reversed) due to changes in the concentration of sodium ($Na^+$), potassium ($K^+$) and chlorine ($Cl^-$) ions. The change in membrane polarity corresponds to a change in the transmembrane current, as shown in Figure 2.1.

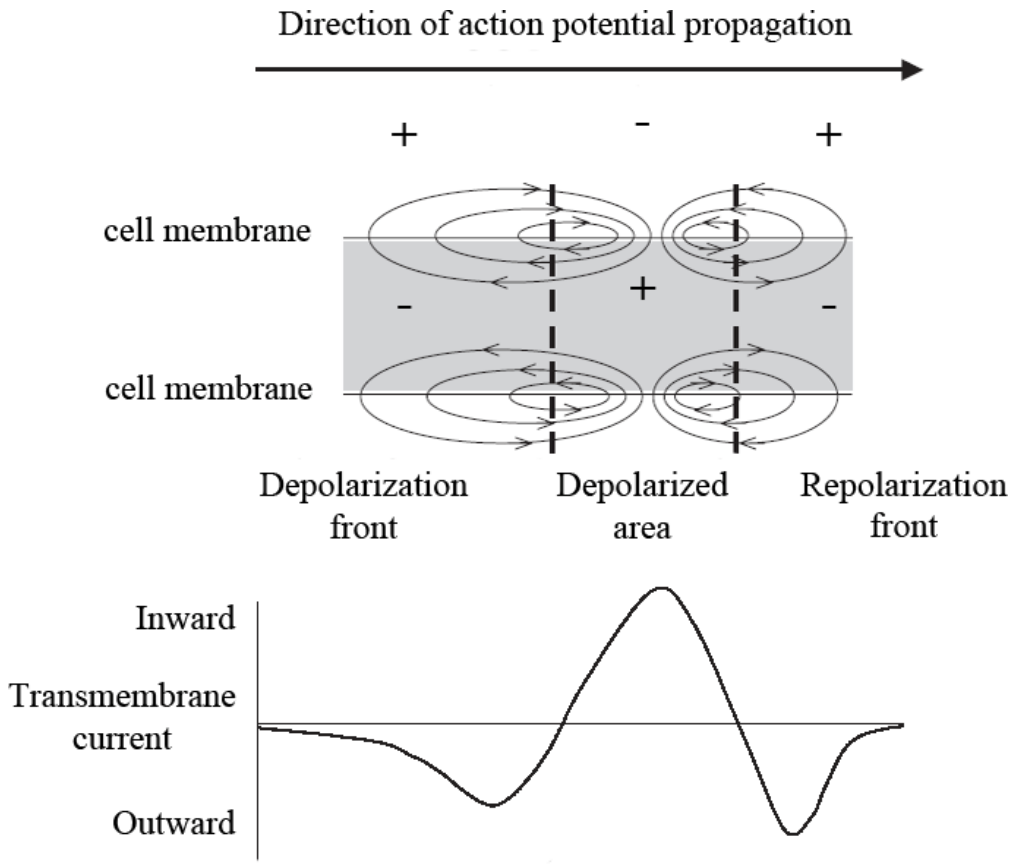


**Figure 2.1 Current flow (depicted as ellipses) during activation of a muscle fibre.**

At the edge of the depolarized region, the transmembrane current will cause the membrane voltage to surpass the threshold for excitation, shown in Figure 2.2.

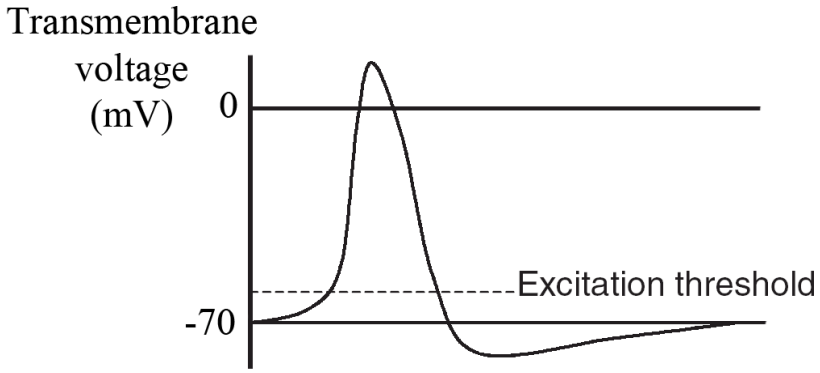


**Figure 2.2 An action potential in an excitable cell.**

Due to the different dynamic behaviour of the $Na^+$ and $K^+$ conductances, the local variation in potential (action potential) will travel along the membrane with a wave-like form. It propagates the length of the muscle fibre and will form an interference pattern with other local AP pulses. This superposition of action potentials constitutes the detected EMG signal.

The amplitude of the EMG is inversely proportional to the size of the detection surface and the uptake radius of the recording electrode. Therefore it can range between tens of microvolts to tens of millivolts depending how it is measured.

The frequency content also depends on several factors. The tissue has a low-pass filtering effect on the signal, where higher frequencies are attenuated significantly more than lower ones with increasing distance between the AP source and the detecting electrode. Consequently the frequency content by needle detection (up to 10 kHz) is much higher by surface detection (up to about 500 Hz) [30].

The signal also has physiological significance: the force of a voluntary muscle contraction is proportional to the number of MUs activated (recruited) for the action as well as their activation frequency. The EMG is further influenced by individual muscle fibre potential, degree of MU discharge synchronization, and fatigue [30].

## 2.5 Existing Methods for EMG-based Prosthesis Control

### 2.5.1 Direct Control

There are generally three approaches to EMG-based prosthesis control [28]. The first and most basic is the idea of controlling a prosthesis action directly with the signals from residual muscle. Current commercially available myoelectric devices operate in this way using skin-surface EMG sensors, and typically the actuation speed of the prosthesis is made proportional to the difference between two EMG signals. With this form of direct control, the user must learn to associate a particular muscle activation to a specific prosthesis function. The muscle to be used is chosen in advance through consultation with a rehabilitation professional for best signal strength and ease of activation by the user, who is trained to reliably flex (activate) this muscle. This is easier to do if the muscles used for EMG signals are physiologically close to the original muscle used for the motion. However, it is often not possible to link a motion to a muscle in a meaningful way. Furthermore, there is a limit to the number of independent surface EMG sites available on a residual limb. The authors of [1] suggest a maximum of four. Consequently the direct control approach described above would not be applicable to advanced prosthetic devices having multiple DOF.

### 2.5.2 Pattern Recognition

The majority of amputees usually have the sensation that their hand still exists, referred to as a phantom feeling [12]. When encouraged to move or flex the phantom limb, a relatively distinct pattern of EMG activity is observed for different intended movements.

If a pattern is recorded for each desired movement, it may later be recognized by a control system, and then used to drive prosthesis motion. There has been significant research into signal processing algorithms for this application, with some achieving a good degree of pattern classification accuracy [32-35]. The earliest approaches required significant processing time to achieve only reasonable accuracy using statistical classifiers on amplitude features. More recently, strategies such as neural networks [36], [37], fuzzy logic [38], linear discriminant analysis [39], machine learning [40], and a wavelet-based approach [41] have been applied to this pattern classification task.

To maximize classification accuracy, a surgical technique has been developed to obtain more numerous and isolated EMG detection sites [26]. This procedure redirects remaining arm nerves by transplanting them onto muscles in the chest and upper arm. It was shown to allow simultaneous operation of only two joints when the user performed a reaching task, and the action was not intuitive.

Regardless of where the EMG is obtained, simply linking an EMG pattern to a prosthetic motion is not true simultaneous control of multiple DOF, so it cannot provide the ability of dexterous manipulation. A recent overview of myoelectric control systems [42] affirms three major weaknesses of pattern recognition control: the lack of a bi-directional interface, the lack of individual DOF control, and its need for a potentially lengthy user learning period (non-intuitive experience).

### 2.5.3 Internal Model using Forward Dynamics

The deficiencies of the methods described above have prompted interest in a more complex but potentially rewarding approach. This is the use of an "internal model" [43-45], which incorporates an anatomically correct musculoskeletal model with forward dynamics simulation. Such a model can predict hand and finger positions, forces and joint torques given a set of individual muscle activations [46]. Application of the internal model to the control problem could offer a truly intuitive user experience that has been absent to date, while providing the ability of dexterous manipulation, all without extensive training.

The idea has been implemented for the control of a seven DOF exoskeleton, though not in real time [47].

## 2.6 Need for Implant-Based EMG Measurement

The forward dynamics model of the arm and hand described above promises to provide intuitive control for a multi-DOF prosthesis, but requires as inputs the activations of individual muscles to a realistic model. In the arm, these activations contribute to the surface-detected EMG measured with electrodes on the skin [30], [34], [40], [48-50]. However, this surface EMG contains significant crosstalk between sensor locations.

### 2.6.1 Crosstalk

Crosstalk is the signal detected over one muscle that was generated by another muscle nearby, and occurs in surface recordings because the distances between sources and detector are similar. There are 18 muscles in the forearm related to the control of the hand and wrist [28], most of which are shown in Figure 2.3.

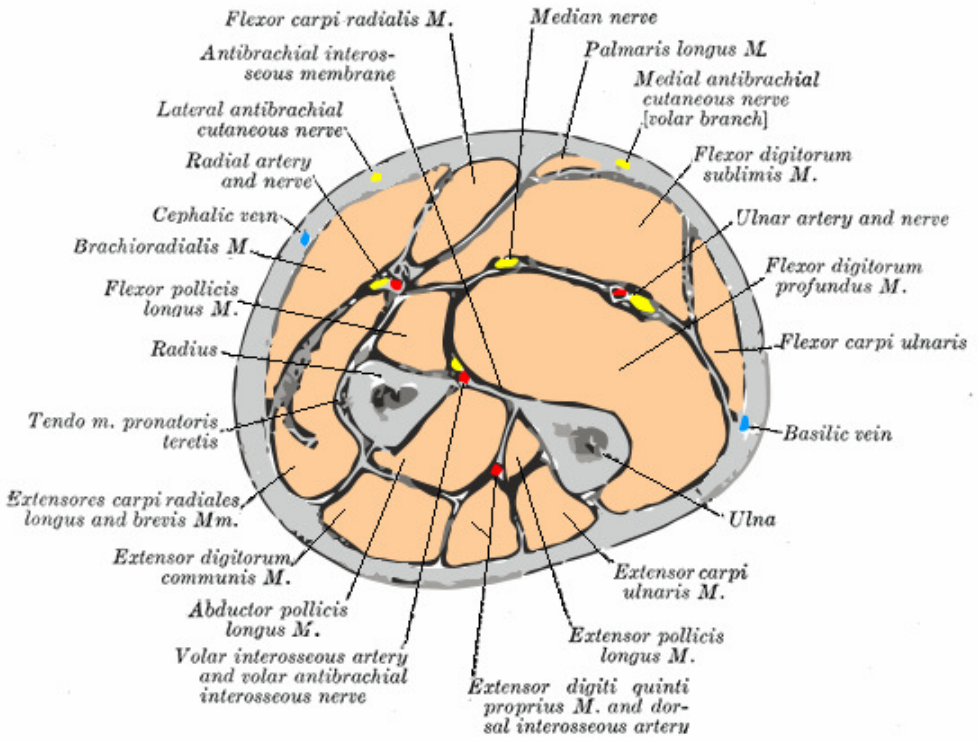


**Figure 2.3 Cross-section through the middle of the forearm [51]**

Crosstalk causes a significant source of error when predicting muscle activations using surface EMG, because it may appear that a muscle is active when actually it is not. Identification of crosstalk sources is hampered by the effect of tissues separating the sources and the detecting electrodes. Besides the variation of tissue shown in Figure 2.3,

the muscles themselves are not homogenous throughout their interior. Figure 2.4 illustrates the hierarchical structure of a muscle.

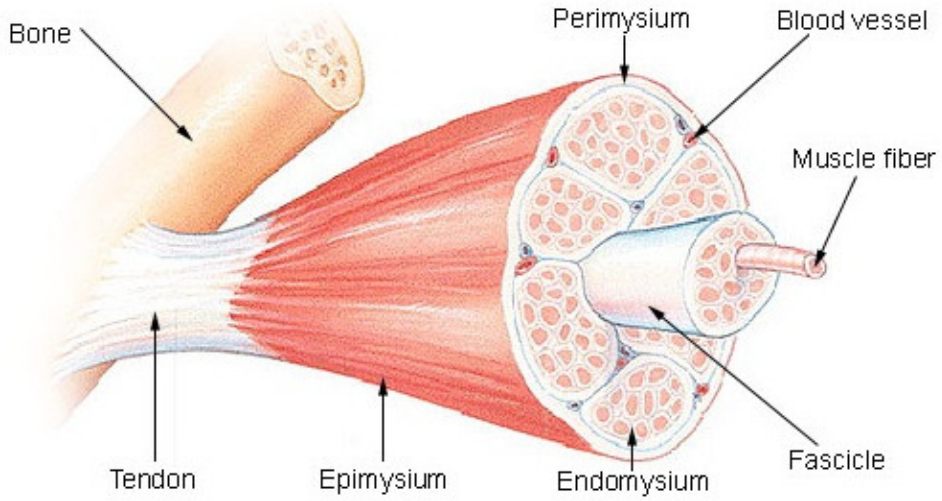


**Figure 2.4 Connective tissue sheaths of skeletal muscle [52].**

Fibrous protein (collagen) sheaths of differing density are interspersed between the muscle fibres. The finest sheaths (endomysium) encase the individual muscle fibres, while progressively thicker envelopes (perimysium) gather the fibres into increasingly larger bundles (fascicles). The outermost layer (epimysium) converges to form tendons for skeletal attachment. Where collagenous tissue is more concentrated, there are relatively fewer muscle fibres. The EMG measured closer to these regions is therefore proportionally smaller [48].

Variation in muscle fibre type is a further factor to the EMG. Overall, the effect of tissue on EMG is that of a spatial low-pass filter [30].

### 2.6.2 Electrode Placement

Besides crosstalk, control schemes using surface EMG suffer from the problem of repeatable electrode placement. The amplitude and spatial content of EMG varies with sensor position due to proximity to the source muscles as well as variation in skin impedance (electrical resistance through the skin). This results in error to the input that the direct and pattern recognition controllers are expecting. Because prosthetic devices may be worn in a slightly different position with each use, and are donned and doffed on a daily basis, it is impossible to guarantee a repeatable sensor position.

### 2.6.3 Intramuscular EMG

It has been demonstrated that intramuscular electrodes allow for the much greater muscle selectivity that is required for more advanced control methods [30], [53]. Intramuscular EMG has traditionally been collected using needle electrodes inserted through the skin, but such a transcutaneous connection is impractical for prosthesis wearers performing daily living activities because tissue skin tissue could be continually damaged, and infection is likely.

Therefore, in the past decade implantable EMG sensors have been in development [28], [54-57], and have recently been demonstrated in animals [1], [39], [58]. EMG measured at the source has a much higher signal-to-noise ratio, and is much less affected by the problems with surface EMG described above. So while surface EMG may be acceptable and arguably preferable for pattern recognition control [33], [34], it is unable to detect individual muscles as well as intramuscular EMG. This means it cannot detect certain natural hand postures that require low muscle effort, or are determined by activations of

the intrinsic rather than extrinsic muscles [49]. Consequently, for more advanced prosthesis control, EMG obtained close to the source is needed.

# 3 Implant Considerations

Having established that intramuscular EMG is required, but that detecting it with needles is not appropriate, the idea of an implanted sensor becomes attractive. Implants, however, have their own range of issues. Primarily, an implant necessitates an invasive surgical procedure for the user, and leads to a significantly increased overall system cost. Further, if the device is too large, it may impact the function of the muscle in which it is implanted. Therefore, one of the objectives is to minimize the overall size of the implant, making it less invasive. Also, if an EMG sensor could be made sufficiently small, it may be possible to simply inject it with a hypodermic needle, as opposed to needing a full surgical procedure.

## 3.1 Implanted Sensor Geometry

To simplify the implantation procedure, the sensor is ideally injected by hypodermic needle into the centre of each muscle of the residual limb (see Figure 2.3) that is needed for the control strategy. Consequently a cylindrical package is envisioned, its axis positioned parallel to the muscle fibres. The detection radius of a sensor with this configuration was simulated in [59] for a 2.5 mm diameter, 15 mm long implanted device. This work represented the implant and surrounding tissue with both a finite-element and analytical model to determine the rate of decay of the EMG with increasing distance of the muscle fibers from the electrode. Then using the analytic representation

of the tissue, the parallel orientation of the implanted sensor was confirmed to be the most selective.

With the sensor dimensions stated above, the authors of [59] found the detection radius would completely fill the smallest arm muscles, suggesting precise implant at the centre of the muscle would be necessary. A smaller package would confine the detection volume even more precisely, increasing selectivity by reducing crosstalk, and decreasing the physical effect of the implant on surrounding tissue.

The most successful implantable EMG sensors to date [1] have been implemented using the existing packaging technology from a muscle stimulator called the *BION* (for bionic neuron). The original design had a glass package [60], [61], based on a similar design from a decade prior [62]. The authors of [63] report on an updated ceramic version of the *BION* with platinum electrodes. The ceramic case was shown to be more rugged, and was able to withstand 8 times the force of the glass package in bend tests [63].

## 3.2 Tissue Response to Implants

Histochemical analysis on the muscle tissue hosting the implant was performed in [63] and no adverse reaction with the body was observed. The same benign reaction occurred for the active or passive implant, as well as a silicone rod studied for comparison. They observed that fibrocollagenous tissue encapsulates the foreign body (ceramic or silicone), in layers from 50 to 100 µm thick.

An earlier study was more expansive [64], evaluating the effect of the constituent materials of an implantable device, including glass, broken glass, suture material, ferrite

and integrated circuit (IC) materials. They observed that the outer encapsulating layer of fibrous, cell-poor material was only 20% of the overall capsule thickness. The rest was an internal accumulation of loosely packed inflammatory cells, typical of the body's healing response to a foreign object. In half of the experimental cases, the total capsule thickness surrounding both active and passive devices was less than 240 µm, and it was never more than 600 µm thick. This tissue response appeared stable over the period of the study (up to 100 days).

### 3.2.1 Tissue Response Effect on EMG

The encapsulating tissue does not negatively affect detection of EMG. Instead, the addition of a highly resistive layer surrounding the electrodes was simulated in [59] to cause an increase in the detected action potential. This result was consistent with previously published simulations for surface EMG [65], [66]. The authors of [59] explain that the increased voltage at the interface of the encapsulation tissue was due to the restriction in current flow in the region surrounding the electrode. Since the current entering the region of high-resistance tissue is small, the voltage dropped across the region is relatively low, yielding a net increase in the potential observed at the recording electrode. In any case, implant circuits have been designed with programmable front-end gain stages [54], which should allow adjustment according to surrounding tissue resistance.

The fibrous tissue also renders the implant immobile in the muscle, which is a benefit to the proposed application, with regards to repeatability of EMG measurement.

## 3.3 Power Level Safety Regulations

Besides the physical effects of implantation due to trauma, those from electromagnetic radiation have been studied as well; [67] and [68] are two reviews cited by other works relevant to the proposed application.

The International Commission on Non-Ionizing Radiation Protection (ICNIRP) is an independent body of specialists that aims to disseminate information and advice on the potential health hazards of exposure to electromagnetic (EM) fields. Their conclusions are founded through evaluation of existing literature, most recently reviewed in [69]. The IEEE standard is compiled in a similar fashion, and attempts to harmonize with the ICNIRP guidelines where scientifically justified [70].

## 3.4 Effects of Electromagnetic (EM) Exposure

The authors of [9] aim to provide a comprehensive summary of the present knowledge about the health effects of EM field exposure. They explain that only the acute effects of electric current inside the body are well understood, where the current corresponds to displacement and/or polarisation of particles through interaction with the electric field.

In the low-frequency range, up to 100 kHz, electric current stimulates nerves and muscles. From 100 kHz onward, heating of the tissue is the predominant effect of exposure. To quantify thermal effects, the commonly used parameter is the specific absorption rate (SAR), which is the amount of power absorbed per unit of mass. The authorities mentioned above specify the exposure limit for frequencies up to 10 MHz for the general public to be five times less than that allowed for occupational exposure, specifically 2 W/kg for the head and trunk of the body, and 4 W/kg for the extremities

(distal to the elbow and knee). A SAR exceeding 4 W/kg averaged over the whole body can overwhelm its thermal regulation capacity, producing harmful tissue heating. Consequently the whole-body average SAR is limited to 0.4 W/kg for occupational exposure or 0.08 W/kg for the general public [71]. Since 1 g of tissue occupies approximately 1 $cm^3$, absorption should not exceed 2 mW in this volume, or similarly, 20 to 40 mW for 10 g of tissue occupying 2.15 $cm^3$.

Numerical methods have been applied to electromagnetic field problems [72]. In particular, the finite-difference time-domain (FDTD) method has been used to investigate the frequency dependence of the SAR on the body [73-75]. These studies determine frequencies at which the SAR was found to be a maximum. The maxima are explained by resonance occurring when there is the strongest coupling between the body and the electric field. The coupling depends on factors including the direction of polarization of the incident wave as well as the height and posture of the body model, which acts in general as a dipole. Consequently, the resonance is different for sitting, standing, adult or child models, or when considering only part of the body. The lowest resonance frequency reported, 35 MHz, is for a whole-body averaged SAR is for the adult male, grounded condition [74]. Smaller volume models (female, child) have higher resonant frequencies. To minimize EM effects on the body, these frequencies suggest an upper limit to the operating frequency of a wireless power system.

An earlier paper used a prolate (egg-shaped) spheroid model to produce an empirical formula for the average SAR over a broad frequency range [76]. The authors noted that in the near-field region, the SAR is approximately proportional to the square of frequency

( $f^2$ ). This result is cited in [77], and further reinforces the case for keeping the operating frequency of the wireless power link below 100 MHz.

## 3.5 Near Field Region

Coupled induction coils provide best performance in the near field region. The near field refers to the electromagnetic field when the distance to the source is less than approximately one tenth of the wavelength ( $d < \lambda / 2\pi$ ). Within this region, the full electromagnetic field equations may be reduced to quasi-stationary approximations and the radiating field can be disregarded. An implant located at the centre of a residual limb, powered from a coil worn on the limb, would be separated from the source by the radius of the coil or a distance of approximately 5 cm. Consequently, in this case the total field is approximated by the near field up to a frequency of nearly 600 MHz ( $\lambda = 0.5$ m).

## 3.6 Influence of Tissue on Inductive EM Field

The components of the electric field, the conservative and non-conservative parts, are affected differently by the properties of tissue. The conservative component $\mathbf{E}_c$ is normally small enough to be negligible inside tissue, when compared to its strength in air outside of the tissue. This is because conductivity and permittivity of the tissue are orders of magnitude larger than for air [78]. If located in the near field as described above, the corresponding conduction and displacement currents are insignificant [9].

However, the magnetic permeability $\mu$ of tissue is practically equal to the permeability of free space $\mu_0$, so a time-variant magnetic field penetrates the body and induces the

non-conservative electric field $\mathbf{E_m}$. This component of the field can be orders of magnitude larger than $\mathbf{E_c}$ explaining why wireless power systems for tissue-implanted devices employ inductive rather than capacitive coupling [9].

The induced electric field causes conduction and displacement currents, which couple it to the magnetic field according to the Maxwell-Ampère law. This law states that the line integral of the magnetic field $\mathbf{H}$ over a closed contour $C$ is equal to the conduction current $\mathbf{J}$ plus the displacement current through the surface enclosed by the contour, $S_C$. In time-domain, integral form, the relationship may be written as:

$$\oint_C \mathbf{H} \cdot \mathrm{d}\mathbf{l} = \int_{S_C} (\mathbf{J} + \frac{\partial}{\partial t}\mathbf{D}) \cdot \mathrm{d}\mathbf{S} \tag{1}$$

However, at low frequencies, the eddy (conduction) and displacement currents are generally too small to disturb the source magnetic field significantly, so the fields may be calculated as if the body was air. The authors of [9] comment on the difficulty of establishing the frequency below which this approximation is acceptable, citing factors including the type and dimensions of the tissue involved. They state that often the displacement current term is negligible against the induced conduction current. Considering the Maxwell-Ampère equation (1) in conjunction with Ohm's law,

$$\mathbf{J} = \sigma \mathbf{E} \tag{2}$$

and the constitutive relation,

$$\mathbf{D} = \varepsilon \mathbf{E} = \varepsilon_r \varepsilon_0 \mathbf{E} \tag{3}$$

then the condition for the above approximation is

$$\sigma \gg \omega \varepsilon \tag{4}$$

For muscle tissue, this condition (4) holds for frequencies up to 100 MHz [78], [79]. If less conductive tissues are present the frequency may be lower. Therefore, for the reasons detailed above, the near field is a good first-order approximation at low frequencies [9].

The authors of [80] recognize the above assumption has been popular in the design of wireless power systems, but with the goal of determining an optimal frequency for this application, they insist the displacement current can not be neglected. Then treating the tissue as a lossy dielectric, they propose an optimal operating frequency of a few GHz in order to maximize the ratio of power received at the implant to power absorbed in tissue. This higher frequency implies a regime somewhere between the near field and far field regions.

## 3.7 Frequency Selection

The approach described in [80] to maximize the power transfer to an implant in tissue by using GHz excitation frequency appears reasonable but is dismissed for the present application primarily in the interest of achieving a practical circuit design. There are a few concerns with using frequencies in the low GHz for power transfer, as follows.

The low end of the microwave spectrum (300 MHz) marks the point at which many of the familiar radio frequency (RF) circuit design techniques become ineffective. The dimensions of the circuit components are no longer small compared to the wavelength, parasitics become significant, and the concepts of inductance and capacitance lose their identity [81]. More comprehensive models that include ground planes, fringing fields, proximity effects and conductor thickness are necessary [82]. Besides introducing

unnecessary complexity to the circuit, power transfer with GHz frequencies has yet to be demonstrated in the literature, whereas many systems operating under 100 MHz have been described [8], [29], [83], [84].

In particular, the wireless power transfer system in [85] operates at 13.56 and 27 MHz, which are frequencies designated in the industrial scientific medical (ISM) bands. These bands were originally reserved internationally for the use of RF energy in purposes other than communications. Applications including electrical discharge machines, microwave ovens or induction heating devices for industry or medicine can create electromagnetic interference that would disrupt radio communication, so their operating frequencies were limited to the ISM bands. Operating in these bands, devices must generally accept interference, but there is no cost or license needed. Because there are also many useful RF communication devices that operate only at short distances, or are tolerant to interference, these applications find good value and near universal operability around the world in the ISM bands. Besides wireless local area networks (LAN) and cordless phones, radio frequency identification (RFID) technology makes use of these bands. Designing implantable devices to operate with the same frequencies allows the large amount of RFID knowledge to be exploited. For example, many of the design approaches for RFID [86], [87] are the same taken with implanted circuits [9].

Therefore, with respect to these issues, conventional frequencies of 300 kHz, 700 kHz and 6.78 MHz have been investigated in this work. These have the benefit of avoiding the range where the absorption in tissue is highest (see section 3.4), and a lumped circuit model should be reasonably accurate [88].

# 4 Wireless Power Transfer

Given the need for intramuscular EMG detection, and that an implanted sensor is being considered to do this, the topic of powering such a device is presently addressed. Operating power may be obtained wirelessly, from an alternating magnetic field supplied by an external coil. This inductive link is preferred to a capacitive or conductive link because the circuit is surrounded by tissue, a lossy dielectric, as described in section 3.6.

For an implantable EMG sensor, a wireless power connection does not suffer from the problems associated with needle connections that are prone to infection, or batteries that take up significant space and require periodic replacement.

Besides sensors or stimulators implanted in muscles or nerves [6-8], inductive coupling has recently been demonstrated for a wireless drug delivery system [3], for powering artificial hearts [2], [4], and has been investigated for applications of a capsule endoscope [89] and retinal prostheses [90].

## 4.1 Coil Configuration for Wireless Power for Implant System

Figure 1.1 illustrates the intended arrangement of the external (primary) coil and the implanted (secondary) coils, for the proposed application of this work. The external transmitting coil is envisioned to encircle the residual limb by being incorporated into the socket of the prosthesis, while the EMG sensors would be implanted into the muscle bundles inside the residual limb (see Figure 2.3).

Accordingly, some general design parameters may be established: To fit within a typical adult prosthesis socket, the primary coil would be approximately 10 cm in diameter, and up to 10 cm in length. The receiver coil would be a much smaller solenoid, approximately 2 mm in diameter, and would always be positioned inside the primary coil. When implanted, it is presumed the secondary coils may be located at any possible position or orientation within the primary, but approximate alignment of the long axes (parallel configuration) is preferred, and is likely the orientation to be used, given the structure of muscle (see Figure 2.4).

**Table 4.1 Proposed Design Parameters for Implantable EMG System**

| | |
|---|---|
| Primary Coil Diameter (cm) | 10 |
| Primary Coil Length (cm) | 10 |
| Primary # of Turns | 14, 150 |
| Primary Wire Diameter (mm) | 0.660 |
| Secondary Coil Diameter (cm) | 0.2 |
| Secondary Coil Length (cm) | 1 |
| Secondary # of Turns | 50, 100 |
| Secondary Wire Diameter (mm) | 0.147 |
| Operating Frequencies (MHz) | 0.3, 0.7, 6.78 |

The requirement for solenoids precludes the coupling enhancement possible with "pancake" spiral coils [91]. However, since the envisioned secondary coils will have some axial offset with respect to the primary coil, as illustrated in Figure 1.1, it has been shown that solenoids are favoured [92] for such a configuration. Relative to the primary, the small diameter of the secondary means it will be loosely coupled to the transmitter circuit, allowing some simplification of the coupling circuit model and analysis [9].

## 4.2 Lumped Circuit Inductive Link Model

Inductively coupled coils can be modelled with lumped parameters [9], [29], [77], [93-104], where the external coil and power source forms one side of a loosely coupled transformer circuit, and the internal coil with load constitutes the other side, as shown in Figure 4.1. A comprehensive introduction to inductively coupled circuits is provided in the classic *Radio Engineer's Handbook* [105] by Terman, but a more modern resource is found in the recent works by Lenaerts and Puers [9] or Van Schuylenbergh and Puers [104].

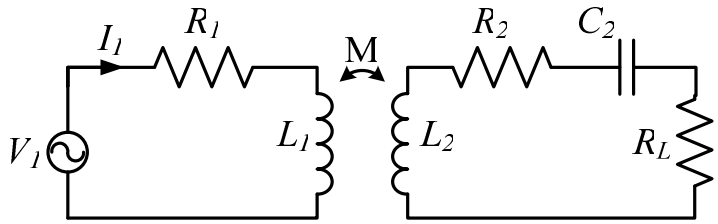


**Figure 4.1 Lumped element model of coupled circuits**

In the lumped circuit model of Figure 4.1, $V_1$ is a sinusoidal voltage source with radian frequency $\omega$, $L_1$ is the self-inductance of the external primary coil, and $L_2$ is the self-inductance of the implanted secondary coil. The resistors $R_{1,2}$ represent the equivalent series resistance of the primary and secondary coils, respectively, as well as any other losses such as energy radiated or lost through tissue absorption. The load resistor $R_L$ represents the implant sensor circuit including losses from voltage regulation and rectification. Capacitor $C_2$ is introduced to secondary circuit to create resonance. This is discussed in section 4.4.

In the lumped circuit, the transmitting (primary) and receiving (secondary) coils are modelled as pure inductances with series resistance. A more accurate representation is the resistor-inductor-capacitor (RLC) combination in Figure 4.2 (where $s = j\omega$), but an equivalent, frequency-dependent $R'$ and $L'$ series combination is appropriate when operating below the self-resonant frequency (SRF) of the coil.

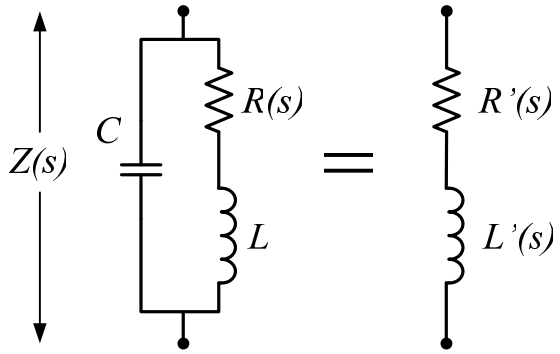


**Figure 4.2 Coil modelled as series RL circuit below self resonance**

The effective $R'$ and $L'$ are dependant on the frequency of the current in the coil, due to the physical geometry of the conductor. For wire cross-sections much smaller than the coil diameter, the effective $L'$ is relatively stable. However, the current distribution across the wire cross-section is dependant on the operating frequency, which causes a variation in $R'$ that generally cannot be neglected.

In a good conductor (such as copper wire used here), the ac current density distribution decreases exponentially from the surface toward the centre of the wire, and this tendency is called the *skin effect*. In other words, most of the current flows between the surface and the first *skin depth*, defined as the depth at which the current density is $1/e \cong 0.368$ its full value. The skin depth $\delta$, may be calculated as $\delta = 1/\sqrt{\pi f \mu \sigma}$ where $f$ is the

frequency, $\sigma = 1/\rho$ is the conductance, and $\mu$ is the magnetic permeability. The skin effect causes the effective resistance of the conductor to increase with frequency (as the skin depth becomes smaller). The effect arises due to opposing eddy currents induced in the conductor by the changing magnetic field that results from the alternating current.

At a particular frequency, the effective resistance is known as the equivalent series resistance (ESR). The ESR (from ohmic loss in the wire) is often lumped together with losses in the surrounding media, including core material or nearby conductive objects. In the circuit above, it includes the losses due to absorption of energy by surrounding tissue, and also radiation that does not reach the implant. These, however, are usually negligible compared to those of the coil conductor, because current in tissue is far smaller than current in the coil wire, as its conductivity is much lower [9], [78] (see section 3.6).

The self-resonance of an inductor is explained as resonance between the inductance and its own capacitance. It is important to consider this behaviour because it defines the upper limit where a series R-L representation of the coil, shown in Figure 4.2, is valid. The left illustration in Figure 4.2, with the parallel capacitance, will model this behaviour (up to the first self-resonant frequency). The capacitance is seen across the terminals of an inductor because there is a voltage and charge density present there. Generally the charge density in a single layer coil increases with its number of turns, decreases with distance between turns, and increases with the permittivity of the medium between turns. Dielectric losses associated with the inter-winding capacitance are usually negligible compared to the losses associated with the inductance [9].

Frequencies above self-resonance are not of interest to the present application because we desire to use the RL model of Figure 4.2. More accurate models could be obtained by

discretization of the inductor into smaller segments, each capacitively coupled with all other segments. The higher the frequency, the more segments that are needed to constitute an accurate model [9], [104].

### 4.3 Self and Mutual Inductance

The self-inductance $L$ for a closed circuit, such as a loop or coil of wire, is defined as: the ratio of the magnetic flux $\Phi$ enclosed by the loop, to the current flowing in the loop that produces the flux. If a second loop is located such that it encloses a portion of the flux generated by the first loop, a mutual inductance $M$ results between them. By reciprocity, the reverse situation results in the same $M$ between loops [106].

The magnetic flux $\Phi$ crossing a surface is the integral of the magnetic flux density $\mathbf{B}$ over that surface. (Consequently, the contributing component of the field is that which is normal to the surface.) The magnetic field $\mathbf{H}$ is related to flux density $\mathbf{B}$ through a constitutive relation similar to that for the electric and displacement fields, (3) above, where the constant electric permittivity is replaced with magnetic permeability:

$$\mathbf{B} = \mu\mathbf{H} = \mu_r\mu_0\mathbf{H} \tag{5}$$

During the inductive coupling effect, the magnetic flux produced by an alternating current in the primary coil penetrates the limb, as described in section 3.6, and this flux is captured to some extent by the secondary coil. (Captured meaning a portion of the magnetic field is enclosed by the secondary coil.) In this way, the two coils (implanted and external) are considered coupled.

The mutual inductance is often expressed as $M = k\sqrt{L_1 L_2}$ where $k$ is the dimensionless coupling coefficient. This coefficient, ranging between zero and one, is the fraction of the flux generated by the first coil that is captured by the second coil. For fixed coil geometries, $k$ is independent of the coil parameters, so it is often used instead of $M$ to describe the coupling. In [9], the low-coupling approximation is proposed for the following condition:

$$\frac{\omega^2 M^2}{R_1 R_2} \ll 1 \tag{6}$$

### 4.3.1 Effect of a Magnetic Core Within a Coil

As shown in [93], [101], [104] the efficiency of the link is related to the degree of coupling between coils, which is the fraction of flux produced by the primary that is captured by the secondary coil. Coupling may be significantly enhanced by adding a magnetic material with a high permeability to the interior of the secondary coil. A general overview of ferritic material is provided in [107], but the specific properties that depend on composition of the material typically must be obtained from the manufacturer [108].

When the dimensions and distance from the primary are much less than the radius of the primary, it can be assumed that the magnetic field distribution in the vicinity of the secondary coil is uniform. Based on this assumption, the authors of [109] present a formula for $M$ that relies on geometrical parameters, and for the case of a secondary with an air-core, their value is equivalent to the estimations developed in [77], [110]. Then by incorporating earlier work on the magnetization of a rod-shaped geometry [111],

they present an analytical formula for $M$ that takes into account a magnetic core material. In particular, their model considers the complex nature of permeability in soft ferrites. Their result has been used in part in the present work to evaluate the proposed FEM modelling method.

## 4.4 Resonant Tuning

The maximum inductive coupling power transfer between a source and a load occurs when their impedances are matched (more specifically they are complex conjugates). This fact is employed for this application, to increase the efficiency of the inductively coupled link. To match the inductive reactance of the secondary coil, a series capacitor $C_2$ is introduced to the secondary coil as shown in Figure 4.1 and 4.3, chosen for resonance at the desired operating frequency $\omega$.

With $C_2$ correctly selected, its reactance cancels with the inductive reactance, leaving only real impedance (resistance) resulting in a resonant circuit. By matching resistances in the secondary, ideally with $R_L = R_2$, maximum power transfer will occur.

The resonant capacitor could also be added in parallel [112], [113], and the comparison between series and parallel forms is discussed in [101], [102].

The primary circuit in Figure 4.1 and 4.3 is somewhat simplified, showing only the primary coil impedance and voltage source. An actual transmitter coil driver circuit is usually some type of switched-mode circuit where energy is pumped into a resonant tank that may be operating at a frequency slightly higher or lower than the transfer frequency. These drivers are discussed in greater detail in [104].

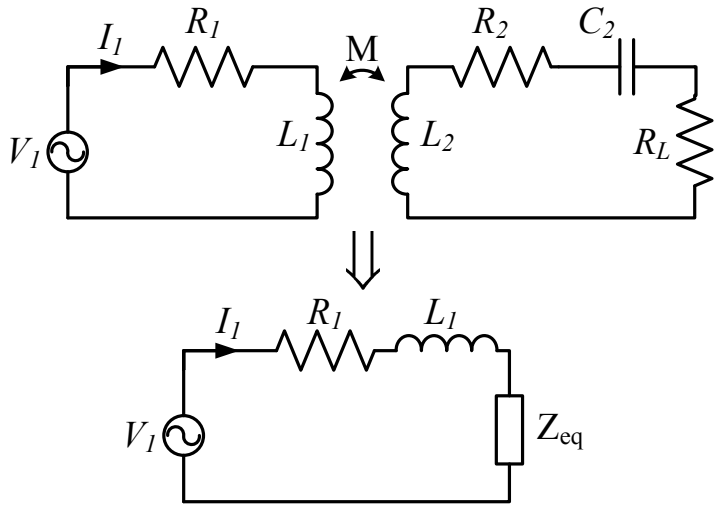


**Figure 4.3 Lumped element model of coupled circuits with equivalent load seen at the primary side**

As shown in the bottom of Figure 4.3, the secondary side of the inductively coupled circuit can be transferred to the primary through the use of an equivalent impedance $Z_{eq}$ [9], [77], [83], [86], [93], [97], [104]. For a series resonant secondary, the equivalent impedance is purely resistive:

$$R_{eq} = \frac{\omega^2 M^2}{R_2 + R_L} \tag{7}$$

Using this case, the authors of [9] calculate the maximum power supplied to the load for a given primary coil current as,

$$P_{R_L Max} = \frac{I_1^2 \omega^2 M^2 R_L}{2(R_2 + R_L)^2} \tag{8}$$

As mentioned above, it is apparent from equation (8), that the load receives maximum power when $R_L = R_2$.

## 4.5 Obtaining the Lumped Circuit Parameters

Equation (8), the power supplied to the load (implant circuit) at resonance, requires knowledge of the various lumped parameters associated with the coupled coils. The equivalent series resistance of the secondary coil $R_2$ appears in the formula, as well as the mutual inductance *M* between the coils. Additionally, the selection of capacitor $C_2$ for resonance depends on the secondary inductance $L_2$. It is chosen according to equation (9) where $\omega_0$ is the radian resonant frequency:

$$\omega_0 = \frac{1}{\sqrt{L_2 C_2}} \tag{9}$$

To determine these circuit parameters, the physical geometry of the coils must be established, including wire gauge and number of turns. For the proposed implantable EMG sensor, the design parameters of the coils are summarized in Table 4.1.

Next, the losses on each side of the transformer circuit should be determined at the operating frequency. As explained above in section 4.2, the losses from wire resistance of the transmitting and receiving coil (ESR), are the most significant. Less significant are losses due to power dissipated in the tissue or due to radiation that does not reach the implant.

### 4.5.1 Experimental Methods

The lumped parameters needed for the circuit model described above are most accurately obtained by experimental measurement of prototype coils. The various

methods and considerations for measuring complex impedance are covered extensively in the *Impedance Measurement Handbook*, [114].

Often the preferred measurement method is the use of an impedance analyzer or LCR meter, which typically employs an auto-balancing bridge circuit internally. This uses a vector voltmeter switched frequently to measure the difference between voltages at each terminal of the device under test (DUT), which allows the current through the DUT to be calculated, and therefore the impedance measured. This method has the advantage of nearly zero input impedance, while being unaffected by test cable capacitance [114].

Another common piece of RF laboratory equipment is a vector network analyzer (VNA). Although it is possible to use the VNA to measure coil parameters, it is not well suited for the task. It derives the DUT impedance magnitude and phase angle from scattering effects (transmission and reflection), from which the real and imaginary impedance components can be computed. As the coil impedance is mostly reactive, small phase-angle errors result in large errors on the real impedance component. Furthermore, the impedance measurement itself becomes less and less accurate the further its magnitude deviates from the characteristic impedance of the VNA (typically 50 Ω). Therefore, careful calibration of the equipment and proper fixturing of the DUT is required to cancel out effects of test cable impedances. The difficulties in assessing the accuracy of the measurement are well described in [115], [116].

As mentioned in [104], the measurement of the inductance $L$ is rarely problematic as it dominates the impedance $Z_L = R_L + j\omega L$. Also as described in section 4.2, the effective $L$ at a particular frequency is nearly the same as its direct current (dc) value. The ESR,

however, is more difficult to measure. Up to a point, these parameters can completely describe the coil, so they are often combined into another parameter, called the quality factor ($Q$), for comparison and circuit analysis. It is defined as ($2\pi$ times) the ratio of the energy stored in a resonator to the energy dissipated per cycle. For an inductor, the ratio is the radian frequency times the inductance, divided by the resistance. Because it describes the damping of the resonator, it can also be defined as the ratio of the resonant frequency ( $\omega_0$ ) to the half-power (3dB) bandwidth $\Delta\omega$:

$$Q = \frac{\omega L}{R} = \frac{\omega_0}{\Delta\omega} \tag{10}$$

In the *R-L* inductor model, the *R* in the denominator of (10) is the ESR. Since the *Q* can be measured relatively easily, the ESR may then be extracted. To measure an inductor's quality factor, it is combined with a (variable) capacitor to resonate at the frequency of interest. The ac source driving the circuit is loosely coupled to the device under test (DUT) through an additional coupling coil (few turns). This configuration is illustrated in Figure 4.4 and described in [117].

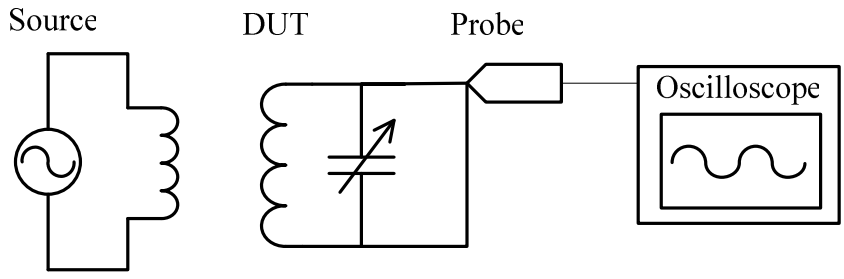


**Figure 4.4 Measurement of coil quality factor (Q) using loosely coupled ac source**

Loose coupling and a high impedance oscilloscope probe are necessary to reduce the effect of the measurement on the circuit of interest. Once the resonant frequency is established, the frequency of the source is varied, and the reduction in voltage across the *LC* combination is observed. The half-power bandwidth can be calculated from the frequencies where the voltage drops to $1/\sqrt{2} = 0.707$ times its maximum, on either side of the resonant frequency.

### 4.5.2 Analytical Methods

Repeated experimental measurement of physical prototype coils obviously becomes costly in terms of time and resources. Consequently, analytical formulas for the calculation of inductance and resistance have been of great interest for RF circuits; see for example [118].

#### 4.5.2.1 Inductance

Of the three passive circuit elements: resistance, capacitance, and inductance, the third is the least amenable to realization in practical devices [119]. As alluded to earlier in section 3.7, the reason is that lumped circuit theory depends on the assumption that the physical dimensions are negligible compared to the wavelength of the incident radiation. For a wound solenoid coil, the problematic dimension is the length of the conductor. Although the wire may be coiled-up into a small volume, its electrical length at radio frequencies cannot be ignored. However, when the assumption above is satisfied, an analytical calculation derived from consideration of the magnetic field alone has

excellent accuracy. The self-inductance may then be determined from the definition mentioned in section 4.3. As shown in [120], the calculation proceeds as follows:

i. Calculate the magnetic flux density $\mathbf{B}$ everywhere

ii. Integrate the flux density to calculate the flux $\Phi$

iii. Multiply by the number of turns ($N$) to obtain the flux linkage $\Lambda = N\Phi$,

iv. Then the inductance is the flux linkage divided by the coil current, $L = \Lambda / I$

Following this procedure, the inductance of a solenoid of length $h$ may be obtained through comparison with a theoretical solenoid of infinite length. In the latter case, the magnetic field outside the coil is (ideally) zero, and the field inside is uniform. Since the wire is small compared to the diameter of the coil, the current can be thought of as a uniform sheet. This cylindrical sheet will have current density $NI / h$ for the solenoid of length $h$. The simple formula (11) is then obtained with the steps above where $A$ is the cross-sectional area of the solenoid.

$$L = \frac{\mu N^2 A}{h} \tag{11}$$

This formula fails if the coil is wound loosely, causing flux leakage. In this case where the flux is not uniform along the coil, Wheeler [121-123] introduced an empirical correction factor. The metric version of his corrected formula for inductance in Henries is provided with the restriction that the solenoid length $l$ should exceed 80% of the radius $r$:

$$L = \frac{u_0 \pi r^2 N^2}{l + 0.9r} \tag{12}$$

Other empirically-derived analytic expressions for inductors of various size and shape, wound with various sizes of conductors, are found in the aforementioned [105] as well as the seminal work of Grover [124-126]. The formulas are summarized well in [120], [127].

#### 4.5.2.2 Limitations of Lumped Parameters

The authors of a much more recent paper (compared to the references above) [128] raise the important reminder that although the preceding formulas are often provided in texts without mention to their limitations, they are really a simplification that relies on uniform current distribution which occurs only at low frequencies. In their earlier work [129], they demonstrate the solution of Maxwell's equations for the field structure and input impedance of helical coils.

More accurately, a coil inductor acts as a complicated transmission line, and the lumped approximation is then just a special limiting case of transmission line theory. This is demonstrated in [128] where using the low frequency (uniform current) approximation, the transmission line terminal point impedance passes to the same value of inductance from (11).

The other passive circuit elements can be thought of in this way as well, but can generally be made small in comparison to wavelength. When they do become large, the distributed parameter models remain fairly simple. Unfortunately, the same is not true for the inductor. The responses at different regions of the electromagnetic spectrum overlap and give rise to interactions between competing propagation processes [119].

The so-called self-capacitance is another consequence of the lumped model being only an approximation. In particular, the notion that the self-capacitance shown in Figure 4.2 is due to capacitance between adjacent turns is only partly true. Counter intuitively, it may in fact increase with coil turn spacing, as reported by the author of [119], who has studied the phenomenon (of self-capacitance) beginning with the earlier analytical calculations [130].

Therefore, to get a sense of the bigger picture of the lumped parameter approach and gain greater perspective on the problem, one is well-advised to become familiar with the concepts presented in [119], [128], [129] first, and to keep them in mind when evaluating the traditional formulas described above.

Fortunately, because inductively coupled links operate below the self-resonant frequency of the coils, the concerns with the lumped model just discussed can mostly be neglected.

### 4.5.3 AC Resistance

A conductor carrying ac current is surrounded by a magnetic field. As the field collapses to reverse direction with each cycle, opposing eddy currents are accordingly induced in the conductor according to Faraday's law, as described in section 4.2. They affect the distribution of the ac current in the conductor, causing it to be greatest near the surface while decreasing towards the centre. This skin effect is significant to the lumped *L-R* inductor model, and has been studied for a long time. The works [105], [131-134] examine resistance at radio frequencies, including the skin effect towards obtaining an

analytical expression. A more recent work by D.W. Knight acknowledges and compares the earlier works, while providing some empirical improvements [132].

An analytical formula for ac resistance may be developed by first considering the formula for dc resistance. For a uniform conductor at low frequencies it is:

$$R_{dc} = \frac{\rho l}{A} \tag{13}$$

where $\rho$ is the resistivity of the medium, $l$ is the length of the conductor, and $A$ is its cross-sectional area. This calculation can be extended to the ac resistance if the cross-sectional area is replaced with a smaller effective area, to account for the skin effect.

This new effective area can be determined exactly using Bessel functions [135], but a much simpler approximation is often useful. This is approximating the effective area by that of a ring extending one skin depth deep into the conductor. This becomes invalid as the skin depth approaches the conductor diameter, but when it is less than the half the diameter, the maximum error in this approximation is 5.5% [132]. Therefore it is a good approximation for relatively thick conductors.

Knight improves on the above approximation by obtaining a modified skin depth from a current density distribution that is truncated at the centre of the conductor. This eliminates the problematic behaviour around the point where skin depth is equal to conductor diameter. The approximation is further improved by noticing the error between it and the exact formula can be fit to a modified Lorentzian function. By using this further correction, the error is reported to be only 0.09%. This seems to be the best ac resistance calculation presently available in the literature. It is preferred to the formula

in the appendix of [104] because it gives the same results, while being defined in a continuous rather than piecewise manner.

## 4.6 Mutual Inductance

The mutual inductance between two coils was defined in section 4.3 as the ratio of magnetic flux enclosed by one coil, to the current producing this flux in the other coil.

It is pointed out in [129] that the analytical development of mutual inductance occurs under the same spatially uniform current assumption discussed in section 4.5.2.2. Consequently the current may be factored out of field integrals, leaving a purely geometrical calculation. The following example illustrates this.

As mentioned above in section 4.3 and shown below in (14), mutual inductance may be calculated as the flux $\Phi$ crossing a surface enclosed by a secondary coil (surface integration of flux density) divided by the current in the primary $I_1$, generating that flux.

$$M = \frac{\Phi_2}{I_1} = \frac{\int_{S_2} \mathbf{B}_2 \cdot dS_2}{I_1} = \frac{\oint \mathbf{A}_2 \cdot d\mathbf{l}_1}{I_1} \tag{14}$$

The flux density may equivalently be calculated from the contour integral of the magnetic vector potential $\mathbf{A}$ according to Stokes' theorem, because $\mathbf{B} = \nabla \times \mathbf{A}$ [135]. This is shown on the right side of (14).

In Figure 4.5 below, the vector potential arising from the current in the filamentary circuit 2 (top) is defined as

$$\mathbf{A}_2 = \frac{\oint \mu I_2 d\mathbf{l}}{4\pi R} \tag{15}$$

Then by substituting this into (14), the mutual inductance between the loops is obtained purely from the geometry, known as the Neumann form [135]:

$$M = \frac{\mu}{4\pi} \oint\oint \frac{d\mathbf{l}_1 \cdot d\mathbf{l}_2}{R} \tag{16}$$

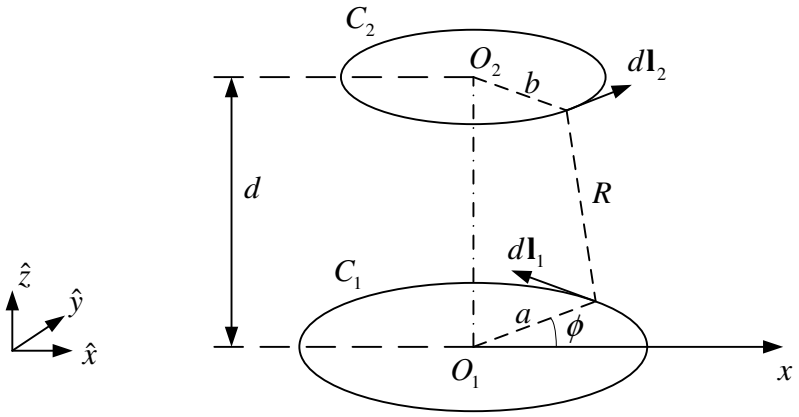


**Figure 4.5 Two circular loops**

When the loops are perfectly aligned, as shown in Figure 4.5, equation (16) may be solved exactly using elliptic integrals, $K(m)$ and $E(m)$ [136]:

$$M = \mu\sqrt{ab}\left[\left(\frac{2}{m} - m\right)K(m) - \frac{2}{m}E(m)\right] \tag{17}$$

where

$$m^2 = \frac{4ab}{d^2 + (a+b)^2} \tag{18}$$

Depending on the geometry, simplification may be appropriate. In [137], it is shown that if the distance between the coils is much larger than the square of the radius of the primary coil, the field at the secondary is uniform (same assumption used in [109]). For

coils with $n_{1,2}$ turns on the same axis, the integration is greatly simplified and the mutual inductance becomes:

$$M = \frac{\mu \pi n_1 n_2 a^2 b^2}{2\sqrt{(b^2 + d^2)^3}} \tag{19}$$

For cases where no simplification from the geometry is possible, the authors of [110] have used (17) to derive approximate formulas when the axes of the loops are laterally and angularly misaligned, as well as the general case for both types of misalignment. Their results are approximate (within 10% of numerical solution) because only the perfect alignment case may be integrated in closed form (although the others may be solved numerically [138]). Their general formula is based on an average of the upper and lower bounds of $M$ and it contains the factor $(\cos\alpha)^{-1/2}$ for an angle of $\alpha$ between the loop axes. In [104] it is explained that this factor is only appropriate for small angles of $\alpha < \pm 20^\circ$ and the coupling is better estimated by a factor of $\cos\alpha$. This latter factor is used in [92], [139] where a power transfer function (gain from transmitter to receiver) is presented for the case of axial misalignment based on analytical evaluation of the magnetic field captured by the secondary coil.

The authors of [104] also comment on the accuracy of the formulas from [110] and they note significant errors result if the coupled coils are not similarly sized. Consequently, this formula was examined and dissmissed in the present work.

Other studies have represented the coil geometry more accurately by extending the current-carrying filamentary rings into two dimensions, giving the coils thickness and height [140], [141]. These works as well as earlier tables [142] are only valid for coaxial

alignments, but more recent work has extended the results to the laterally and axially misaligned cases [143]. Among the analytically-developed methods, the algorithm in [143] is the most representative for the coil configuration of interest.

Essentially the algorithm sums the contribution to mutual inductance from each ring of current in the primary and secondary. However, since only air core coils are accounted for, the effect of magnetic material was included in the present work but multiplying by an additional ferrite factor. This factor was developed recently in [109], but was applied to limited symmetric coil geometry there, and suggested the aforementioned $\cos\alpha$ factor for cases of axial misalignment.

After digitizing the permeability data for magnetic material 3C90 shown in Appendix A, taking $\mu_r = 2510 - j290$ at the frequency of interest, the cylindrical demagnetization factor described in [109] was calculated as $D_{fc} = 3.96\times10^{-9}$.

The multiplicative ferrite factor is

$$\frac{\mu_r}{1+D_{fc}(\mu_r-1)} \tag{20}$$

# 5 Requirements for Computational Modelling Method (Application Requirements)

The focus of this thesis is to create a computational method that can predict the amount of power that would be available to an implanted device. As explained in the preceding chapters, this transmitted power is a function of many parameters that are difficult to model analytically. Besides the frequency and strength of the magnetic field delivering the energy, geometrical variables and material properties contribute to the result. Quantifying these parameters is necessary to determine power transfer efficiency and system viability. Therefore, such a computational approach would be a design tool of great use in the development of implantable devices.

## 5.1 Existing Prediction Method

The consumption of power at the implant is a function of the implanted circuit load $R_L$, and will vary for different applications. For an inductively coupled circuit with a series resonant secondary coil, the authors of [9] presented a formula to calculate the maximum power supplied to a load, for a given primary coil current, as provided in equation (8).

The lumped circuit parameters needed for this formula, introduced in section 4.2, can most accurately be obtained by experimental measurement of physical prototype coils, as described in section 4.5.1, but this method is time consuming and costly if many coils must be constructed during the design process.

Consequently, analytical formulas have been developed in order to compute the values of the lumped circuit model of the inductively coupled coils. These formulas, described above in section 4.5.2, must be selected according to the particular coil geometry of interest, and offer only an approximation. Until recently, no analytical expression existed for the mutual inductance between coils that also accounted for magnetic material in the core. Although one has been recently proposed in [109], the authors presume a uniform field at the secondary and have simply used an approximation factor when the coils are not aligned in the ideal case [110].

## 5.2 Proposed Computational Method and Requirements

Given the existing limitations, it is proposed to model the geometry as well as magnetic properties of a coupled coil system using the finite element method (FEM). With this approach, the mutual inductance for any coil geometry and configuration can be calculated in a timely manner at multiple frequencies without constructing any physical prototypes. Furthermore, with the use of a three dimensional (3D) FEM model, the mutual inductance between two coils for any arbitrary off-axis position and orientation can be found.

The FEM model can be extended to include magnetic core material in the receiver coil by simply changing the physical constants in that volume from air to ferrite. Further, a region surrounding the secondary coil could be defined with the conductivity and permittivity of tissue in order to calculate the SAR (energy absorption) in that location.

Little work has been published on an FEM approach to modelling wound solenoid inductors. A two-dimensional FEM model is described in [9], [10], [144], but a three-

dimensional FEM model for solenoids has not been found in the literature, suggesting the approach is a novel one.

The requirements for this computational modelling method are as follows:

- A reasonable simulation solution time (on the order of minutes).
- The ability to vary physical properties such as secondary core material, or the presence of a nearby lossy dielectric (tissue).
- Determination of the degree of coupling between the primary and secondary coils, as their relative position and orientation is varied in 3D space.
- The ability to vary coil geometries and parameters such as diameter, length, number of turns, wire diameter, and conductor material.
- Flexibility to provide a solution over a range of frequencies.

# 6 Modeling Inductive Coupling with the Finite Element Method

The finite element method is a numerical technique used to solve boundary-value problems characterized by a partial differential equation with boundary conditions. In this approach, the physical domain of the problem is discretized into smaller subdomains in order to express the problem as a system of simultaneous linear equations that can be solved computationally to yield approximate values of the unknowns at a discrete number of points (nodes) within the system. Besides electromagnetics [145], [146], many other physics problems can be described analytically using ordinary or partial differential equations, and may be solved using FEM. By using it to model power transfer between coupled coils, various coil-to-coil orientations, coil shapes and core materials that are normally not considered using existing analytical methods can now be simulated.

## 6.1 Methodology for FEM Model Approach

The results of both two-dimensional (2D) and 3D FEM models are used to determine the lumped circuit parameters in order to calculate power transferred wirelessly to a load representing an implanted circuit.

The process begins by creating a 2D axisymmetric model of each solenoid by defining geometrically the number of turns, diameter, length, and conductor diameter, as well as the spacing between turns. The dimensions for the particular coils constructed and evaluated in this work are listed in Table 6.1.

**Table 6.1 Constructed Coil Parameters**

| side | primary | | secondary | |
|---|---|---|---|---|
| number of turns | 150 | 14 | 100 | 50 |
| coil diameter (mm) | 100 | 100 | 1.94 | 1.5 |
| length (mm) | 106.5 | 95 | 15 | 10 |
| wire gauge (AWG) | 22 | 22 | 36 | 36 |
| conductor diameter (mm) | 0.66 | 0.66 | 0.147 | 0.147 |
| core | air | air | plastic | ferrite |

Also specified is the total current applied to the primary coil, the material properties of the conductor, and the core material. The solution may be recalculated at each frequency of interest and provides the equivalent inductance of the coils $L_1$, $L_2$, and the equivalent series resistances $R_1$, $R_2$, as shown in the circuit of Figure 4.1.

Next, a 3D model is created by directing current in a helical path with the same geometry that the 2D models represent. Additionally, a cylindrical volume representing the implant sensor volume is created somewhere within the space enclosed by the primary coil, and the electromagnetic properties for the secondary core are specified (i.e. ferrite or plastic). The particular ferrite used in the analysis of this work was 3C90 from Ferroxcube. Its properties are provided in Appendix A.

The solution of the magnetic field simulation provides the resulting flux density induced within the secondary ferrite volume. The mutual inductance between coils can then be obtained with post-processing integration. Finally, the power supplied to a matched load (i.e. implanted circuit) can be calculated using equation (8).

## 6.2 2D Axisymmetric FEM Model

A 2D axisymmetric model is created using multiple turns so as to accurately represent the solenoid of interest, and is used to calculate the equivalent ac inductance and resistance. The model was derived from a simpler single-turn example provided in the *COMSOL* FEM software package [147].

The development of the governing equations for this model is explained in [9]. First an external source current density $\mathbf{J}^{\mathbf{e}}$ is added to the Maxwell-Ampère equation serving as an input for the model:

$$\nabla \times \mathbf{H} = \sigma \mathbf{E} + j\omega \mathbf{D} + \mathbf{J}^{\mathbf{e}} \tag{21}$$

Then, using the constitutive relations (3), (5), the definition of magnetic potential from section 4.6, and the electric potential, $\mathbf{E} = -\nabla V - j\omega \mathbf{A}$, equation (21) may be written as:

$$\nabla \times (\mu^{-1} \nabla \times \mathbf{A}) + (j\omega\sigma - \omega^2 \varepsilon)\mathbf{A} + (\sigma + j\omega\varepsilon)\nabla V = \mathbf{J}^{\mathbf{e}} \tag{22}$$

A second equation is obtained by taking the divergence of (22):

$$\nabla \cdot \left[ (j\omega\sigma - \omega^2 \varepsilon)\mathbf{A} + (\sigma + j\omega\varepsilon)\nabla V - \mathbf{J}^{\mathbf{e}} \right] = 0 \tag{23}$$

It is equation (22) and (23) that are solved simultaneously to obtain vector potential $\mathbf{A}$ and electric potential $V$.

The 2D axisymmetric FEM model relies on the symmetry of a helical coil about its long axis, as shown in Figure 6.1. In this axisymmetric representation, current only flows in the $\varphi$ direction (out of page), through and not across the $r$-$z$ plane containing the cross-section of the coil. Consequently vector quantities for current and potential that are

orthogonal to the $r$-$z$ plane are reduced to scalars, and equation (22) is simplified to equation (24) [9], which more closely resembles the form implemented in *COMSOL*.

$$-\frac{1}{\mu}\nabla^2 A_\varphi + (j\omega\sigma - \omega^2\varepsilon)A_\varphi = J_\varphi^e \tag{24}$$

As frequency increases, the distribution of current through the conductor cross-section becomes concentrated towards the exterior, increasing the effective resistance of the coil. This is the so-called *skin effect*. To correctly model this skin effect at higher frequencies, as well as the proximity effect caused by the magnetic fields from currents in nearby turns, the coil cross-section is modelled by circles, as shown in Figure 6.1.

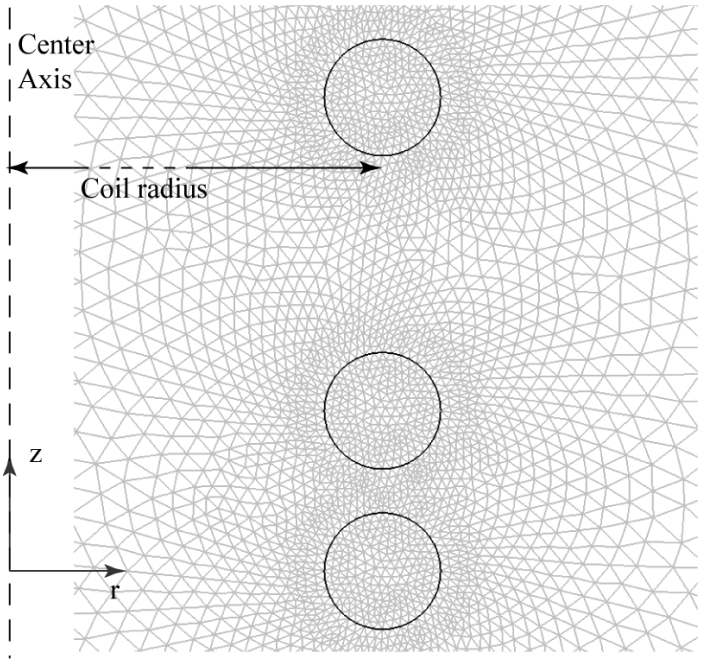


**Figure 6.1 Sample of mesh for axisymmetric FE model of solenoid**

Further, the mesh element size of the conductor cross-section should be at least half the expected skin depth at the frequency of consideration. Note that in the example of Figure

6.1 and Figure 6.2, the various turn cross-sections are not spaced equally in the z-direction, to demonstrate the ability of the FEM to simulate the proximity effect.

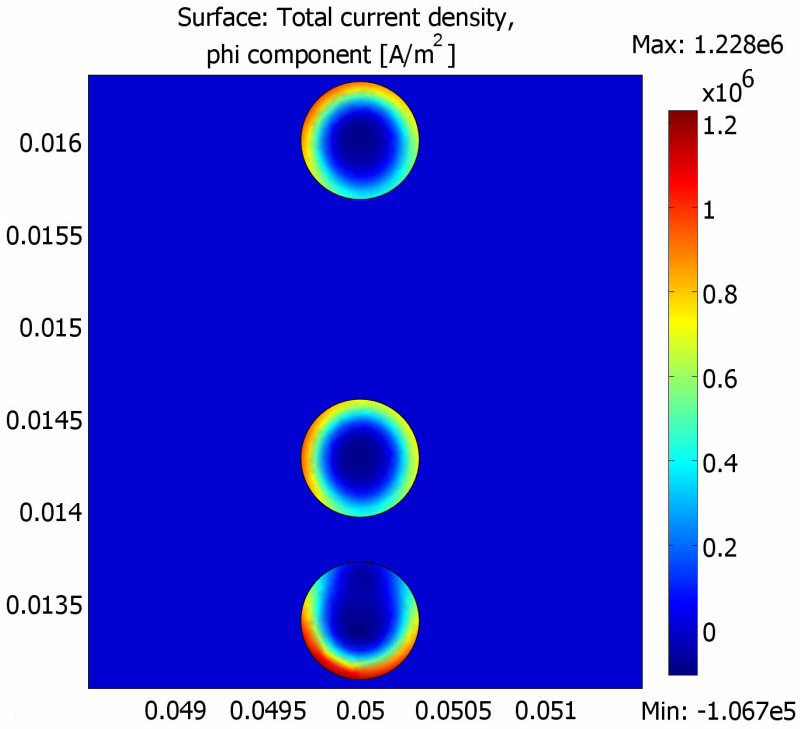


**Figure 6.2 Current density, phi component from 2D FE model**

In the proposed 2D FEM method, the current applied to the coil is an input parameter defined as constant $I_0$. For each turn from 1 to $N$, a subdomain integration variable, $I_1$ to $I_N$ is defined to integrate the current density $J_\varphi$ over the cross-section, and the loop potential is defined in each turn as variable $V_1$ to $V_N$. *COMSOL* provides the ability to define global equations that are solved concurrently to the spatial problem. This feature is employed here: a global equation for each loop voltage from $V_1$ to $V_N$ is defined as $I_N - I_0 = 0$. The consequence is that when the model is solved, the value of the $V_N$ in each turn is adjusted so that the associated global equation is satisfied. The result is a

small variation between the loop potentials, but the same amount of current through each turn. By defining a scalar expression to sum all the loop voltages and divide by the total current, the impedance of the coil is determined:

$$\sum V_N / I_0 = j\omega L + R \tag{25}$$

The resistance may be extracted as the real part of (25) and inductance as the imaginary part divided by $\omega = 2\pi f$. As shown in Figure 6.2, this model predicts current distribution according to skin and proximity effects.

For the example illustrated in Figure 6.1 and 6.2 all the parameters and settings used in the 2D *COMSOL* model are provided in Appendix B.

## 6.3 3D Finite Element Model

The 3D FEM simulation is used to model the magnetic fields and flux density surrounding coupled solenoids. The 3D domain is necessary to model an arbitrarily oriented secondary coil (the implantable sensor), which may be located anywhere inside the primary coil volume.

A common FEM guideline to preserve mesh integrity is to limit the individual and relative aspect ratios of the meshed elements, where [148] has advised caution for using ratios greater than three. Consequently, for successful 3D FEM meshing, large differences in size between the geometry of the various objects should be minimized. For the present application this stipulation was a problem since the primary coil diameter is 50 times greater than the secondary coil diameter, and the conductor diameters are 200 times smaller than the coil diameters.

Initially, *SolidWorks* CAD software was used to create the geometry of the primary multi-turn solenoid. This geometry was imported into *COMSOL* as a true three-dimensional helix, and placed within a spherical boundary domain. Attempts to mesh and solve with this geometry were met with various difficulties. In most cases it was impossible to mesh the solid helix using a coarse mesh due to its radius of curvature, and a fine mesh is actually needed in order to resolve the skin effect on conductor current at high frequencies.

In order to mesh such multi-scale domains, and yet preserve mesh integrity, several million or more 3D elements are required for the simulation. Unfortunately a model with so many elements does not converge on a solution in many cases, or takes an unreasonable amount of time to solve, conflicting with the design requirements set in chapter 5.

As with any complex problem, there must be a balance between simplifying the problem to make it manageable and retaining enough complexity to make it relevant. With this in mind, the solution proposed here is to represent the 3D primary coil as a filamentary current-carrying helix in order to produce the magnetic field within and around the primary coil. Some typical parameters of each model are provided in Table 6.2.

**Table 6.2 *COMSOL* FEM Model Parameters**

| model dimensions | 2D | 3D |
|---|---|---|
| solver | stationary, direct<br>UMFPACK | stationary, iterative<br>GMRES |
| total no. elements in mesh | 196 620 | 106 708 |
| solution time | 12.6 s | 88.5 s |

*COMSOL* 3.5a and 4.0a on Windows 7 64-bit, Intel i7, 12 GB RAM

The primary coil geometry is prepared by using a *MATLAB* script that generates the coordinates of line segments that follow a helical path. (This script is reproduced in Appendix C). The true curvature is more accurately represented using a higher number of segments per turn. The effect on flux produced when the number of segments per primary coil turn was studied, and plotted in Figure 6.3. Here, 41 segments per turn was found to provide an accurate representation with an acceptable computation time.

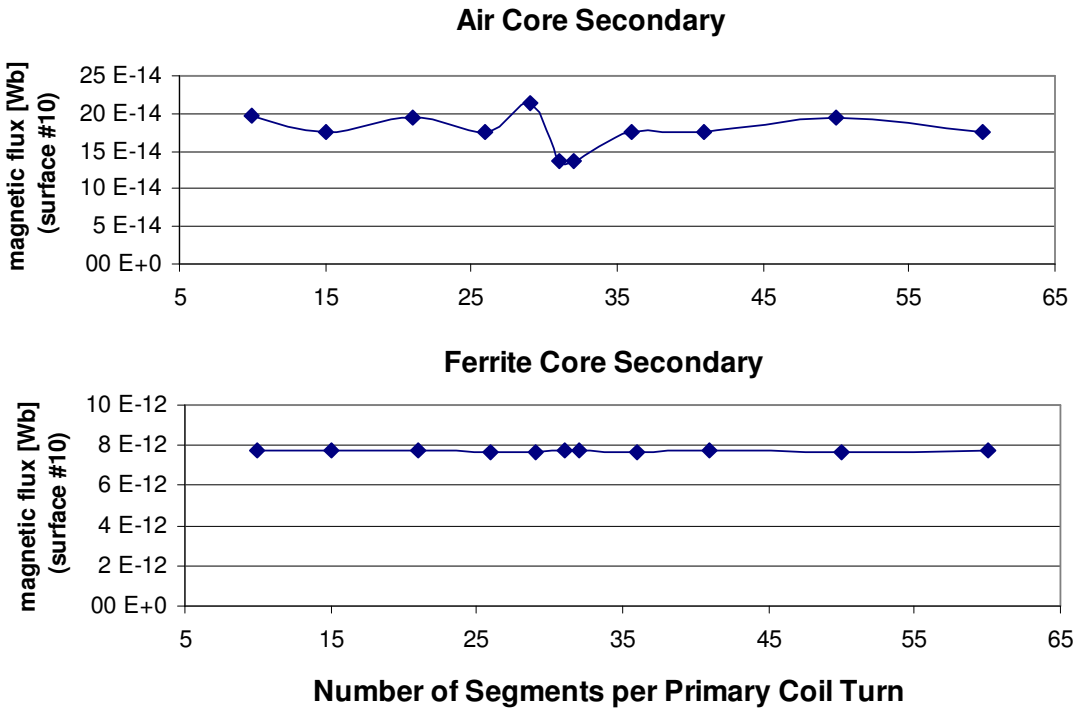


**Figure 6.3 Effect on flux produced by primary coil by varying segments per turn**

*COMSOL* version 3.5a allows the Cartesian coordinates of the segment ends to be copied into the "polyline" geometry tool. The model file was then opened in version 4.0a in order to use its improved interface.

The ac current is an input to the model, defined along the helical path. One must be careful to ensure the segments are all following one direction. This check can be performed by plotting the tangent variables of the line segments as shown in Figure 6.4, where only a fraction are plotted for clarity.

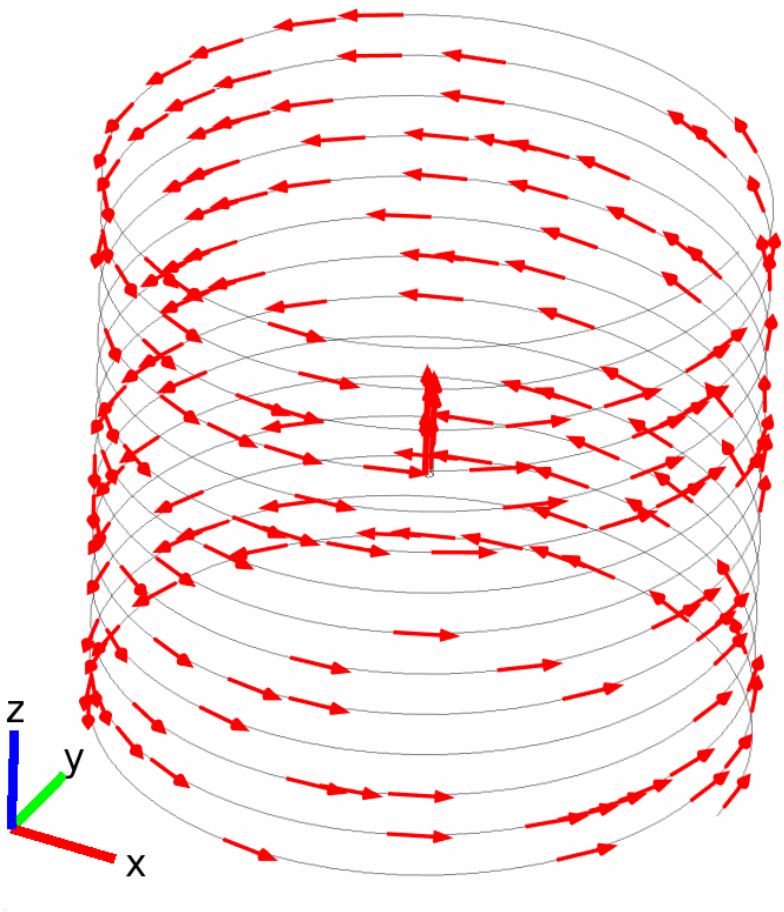


**Figure 6.4 3D *COMSOL* plot of tangent variables for 14-turn primary solenoid indicating direction of applied current**

Ultimately, the quantity of interest from the 3D simulation is the flux passing through the secondary coil. A small cylindrical volume is defined in the 3D model to represent the secondary coil core, but the secondary conductor is not modeled. The material property of this volume is also an input to the model, defined as an air core or ferrite core, and an appropriately small mesh size is imposed on this volume.

In general, the magnetic flux density in the small cylindrical volume will vary along its length. Therefore, the flux density is integrated in the cylindrical volume and divided by its length to determine an average flux being captured by the coil. The total flux linkage

is this average value multiplied by the number of secondary turns, as described in section 4.5.2.1. Then using (8), the power supplied to the matched load (implant) can be calculated given the primary coil current and the ESR of the secondary coil.

A description of the parameters and settings used in the 3D *COMSOL* model is provided in Appendix D.

# 7 Experimental Methodology and Setup

The results of the software-based simulation were verified through testing of physical prototypes of the coils, using the techniques described in section 4.5.1. In particular an HP 4285A LCR meter was used to evaluate the validity of the 2D simulation by measuring the effective inductance and equivalent series resistance (ESR) of all the coils over a range of frequencies that included those of interest (see Table 4.1).

An experiment was also conducted to measure the mutual inductance between the primary and secondary coils, in order to compare with the result of the 3D FEM simulation. In this experiment, the 14-turn primary coil was driven with a sinusoidal voltage produced by a waveform generator (PXI-5412 from National Instruments). The 50-turn secondary coil with ferrite core was centred inside the primary coil (both horizontally and vertically) and aligned parallel to the primary coil axis. This was done by securing the secondary coil to a wooden rod, which was held by a manual x-y-z positioning stage. The experiment apparatus is shown in Figure 7.1

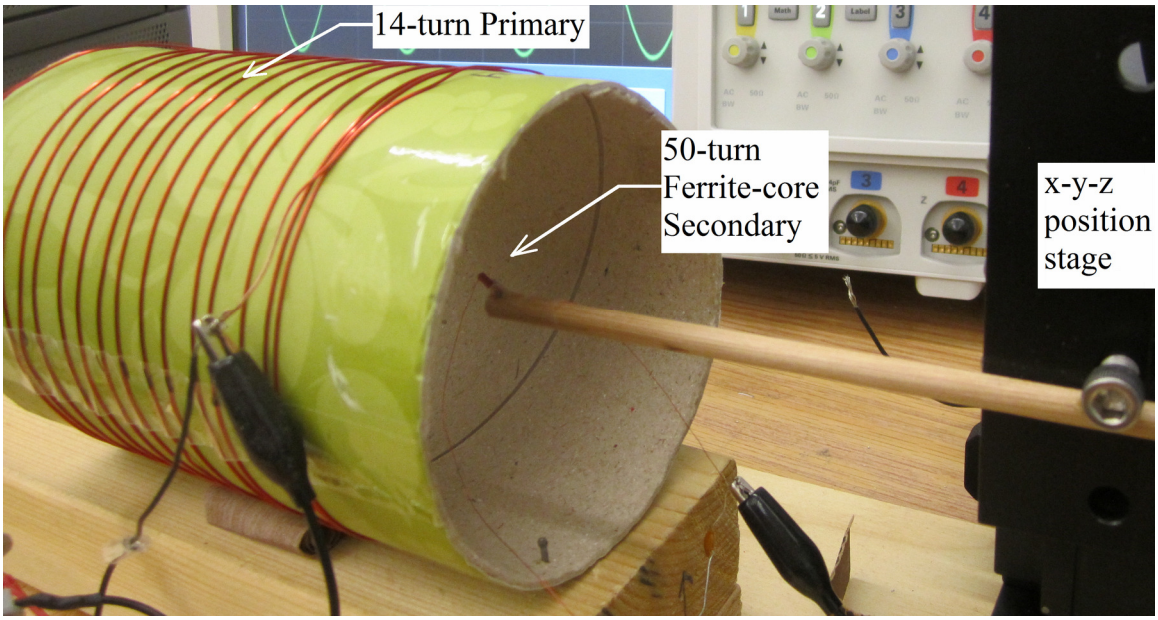


**Figure 7.1 Experimental setup to measure primary and secondary coil voltage**

The secondary coil was positioned at various radial and longitudinal positions within the primary coil, via the x-y-z positioning stage. This included positions centered on the primary axis, as well as 2 cm, and 4 cm radially out from the primary axis. It was also positioned centered along the long-axis of the primary coil, then 2.5 cm from the center, and 5 cm from the center. Finally it was rotated from parallel so that the coil axes were 30° and 60° apart. By combining each of these configurations, $3\times3\times3=27$ positions are obtained, and the voltage across both coils was recorded at each of these positions. Typical waveforms are shown in Figure 7.2 where the voltage was measured across the 14-turn primary (22 AWG) and 50-turn ferrite-core secondary (36 AWG) when an amplitude of 5 V pk-pk is specified in the NI PXI-5412 software front panel. The primary coil is directly connected to the signal generator; the secondary coil is connected to the parallel capacitance described below.

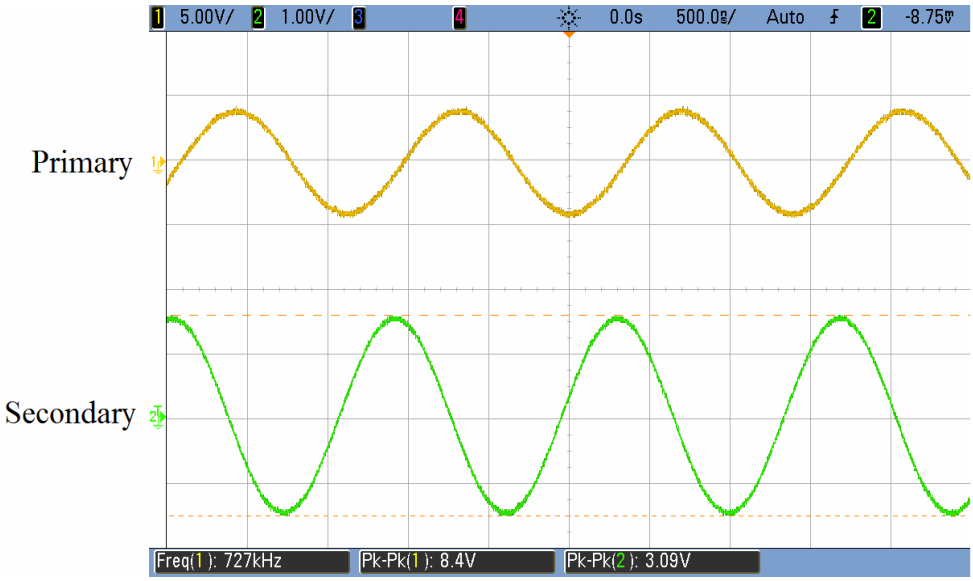


**Figure 7.2 Oscilloscope output of typical coil voltage measurements**

A formula is provided in [86] to calculate the mutual inductance from the measurement of primary and secondary coil voltages. After substituting $k = M / \sqrt{L_1 L_2}$, that formula is

$$M = A_k \frac{V_2}{V_1} L_1 \tag{26}$$

where $V_2$ is the secondary voltage, $V_1$ is the primary voltage, $L_1$ is the primary inductance and $A_k$ is a correction factor:

$$A_k = 2 - \frac{1}{1 - (\omega^2 \cdot C_{TOT} \cdot L_2)} \tag{27}$$

where $C_{TOT}$ is all of the parallel capacitance across the secondary, including parasitic and cable capacitance. In the experiment, a 3 nF capacitor was used in parallel with the secondary to create resonance and increase the stability in the measured secondary voltage (i.e. by reducing the influence of parasitics). The oscilloscope probe adds about 15 pF as well, but this is not significant in light of the resonant capacitor.

# 8 Results and Discussion

The 2D finite-element simulation results of coil inductance and resistance are now compared to values obtained by measurement of the test coils constructed with the dimensions from Table 6.1.

The 3D FEM simulation results for mutual inductance are compared to the values calculated from the measured voltages, obtained as described in chapter 7, as well as the result of analytical formulas introduced in section 4.6.

## 8.1 Measured, Calculated, and 2D Simulated Resistance and Inductance (dc)

The validity of the 2D FEM simulations was initially evaluated by comparison to measurement and formula for the dc case. Referring to the upper half of Table 8.1, it is apparent that the 2D simulation of dc resistance is in close agreement with the simple analytical calculation (where $\rho$ is resistivity) in all cases. The measured dc resistance matches reasonably well for the larger primary coils, but was greater than the calculation and simulation values for the two secondary coils with smaller wire diameter.

**Table 8.1 Measured, Calculated and Simulated dc Resistance and Inductance**

| side of circuit | primary | | secondary | |
|---|---|---|---|---|
| number of turns | 150 | 14 | 100 | 50 |
| $R_{dc}$ measured (Ω) | 2.64 | 0.34 | 1.30 | 0.81 |
| $R_{dc} = \rho \cdot length / Area$ (Ω) | 2.50 | 0.23 | 0.80 | 0.23 |
| $R_{dc}$ *COMSOL* (Ω) | 2.44 | 0.23 | 0.80 | 0.34 |
| $L$ measured (μH) | 1510 | 16 100 | 2.70 | 17.0 |
| $L$ *COMSOL* (μH) | 1480 | 14 700 | 2.23 | 14.8 |
| $L$ Wheeler[a] (μH) | 1470 | 13 800 | 2.35 | (ferrite) |
| $L$ Maxwell[b] (μH) | 1460 | 15 100 | 2.12 | (ferrite) |

[a] using formula (12) from [131]
[b] using *INCA* [149]

As shown in the lower half of Table 8.1 there is very good agreement between measured, simulated, and calculated (Wheeler, Maxwell) values for inductance. The calculation in the last row was generated using the *INCA* software calculator which uses Maxwell's method of calculating the self-inductance using Neumann's formula for mutual inductance between filamental conductors that are separated by their geometrical mean distance [149]. These analytical formulas are for air-core solenoids, so no value is calculated for the 50-turn ferrite-core coil. It is apparent that the inductance of the 100 turn plastic (polyethylene) core can be approximated by the formula, but its resistance cannot.

## 8.2 Simulated vs. Measured Impedance (75 kHz to 6.78MHz)

The following plots (Figures 8.1 to 8.4) compare measured and simulated values for the impedance of the coils. These are expressed with magnitude $|Z| = \sqrt{(\omega L)^2 + ESR^2}$ and phase $\theta = \arctan(\frac{\omega L}{ESR})$ plots.

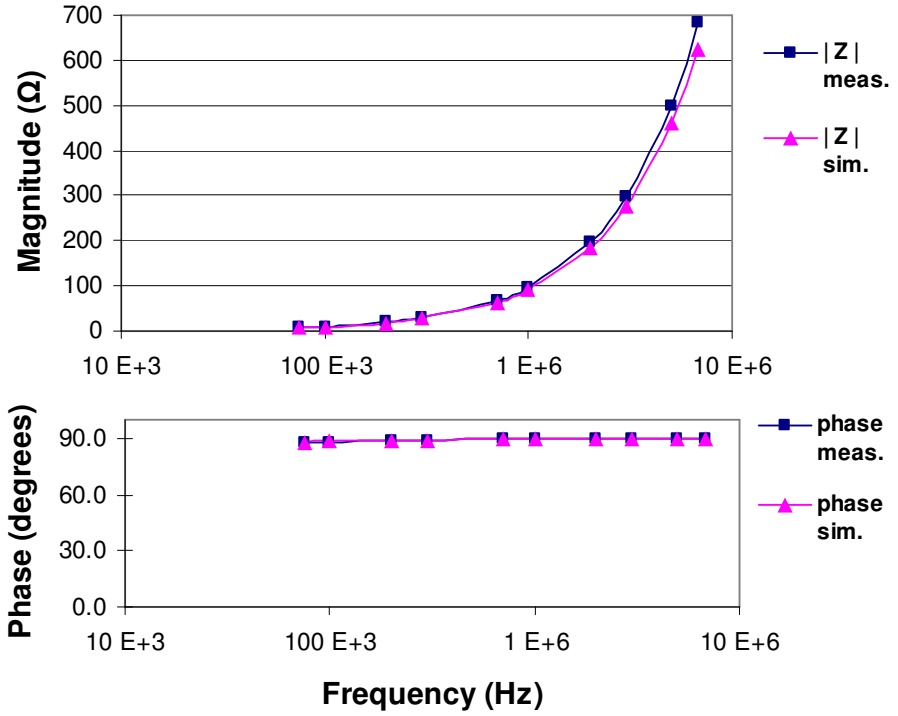


**Figure 8.1 Measured and simulated impedance for 14-turn air core solenoid**

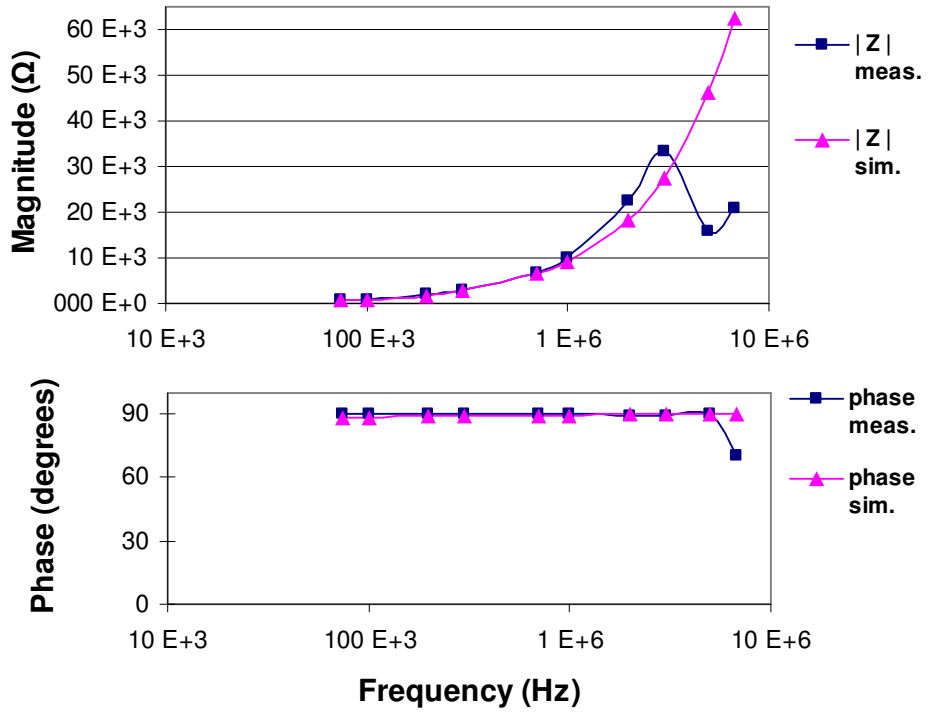


**Figure 8.2 Measured and simulated impedance for 150-turn air core solenoid**

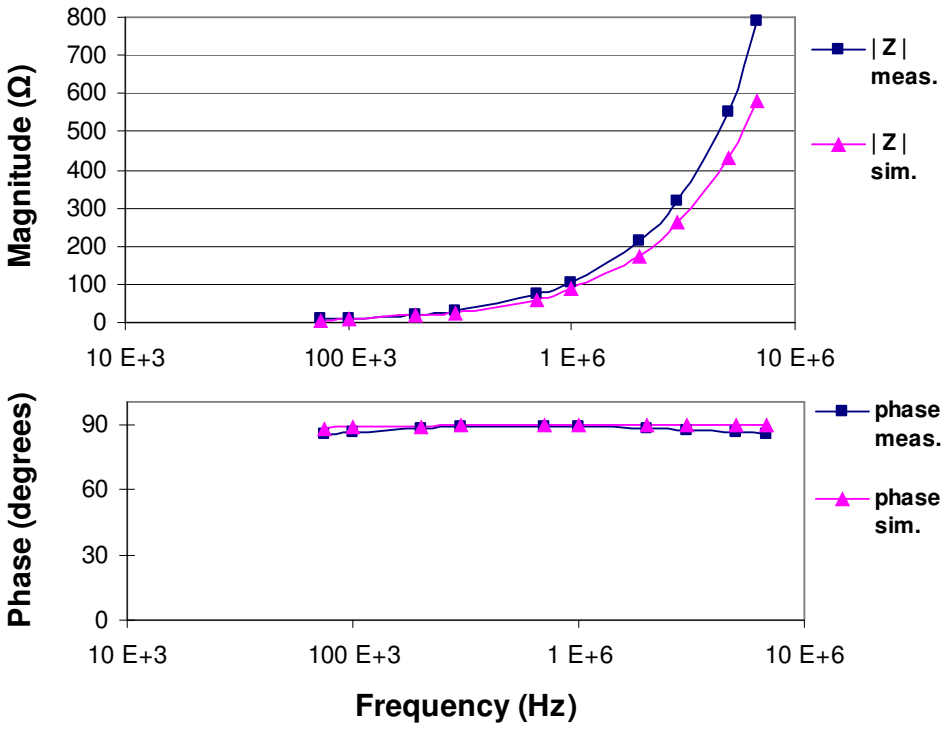


**Figure 8.3 Measured and simulated impedance for 50-turn ferrite (3C90) core solenoid**

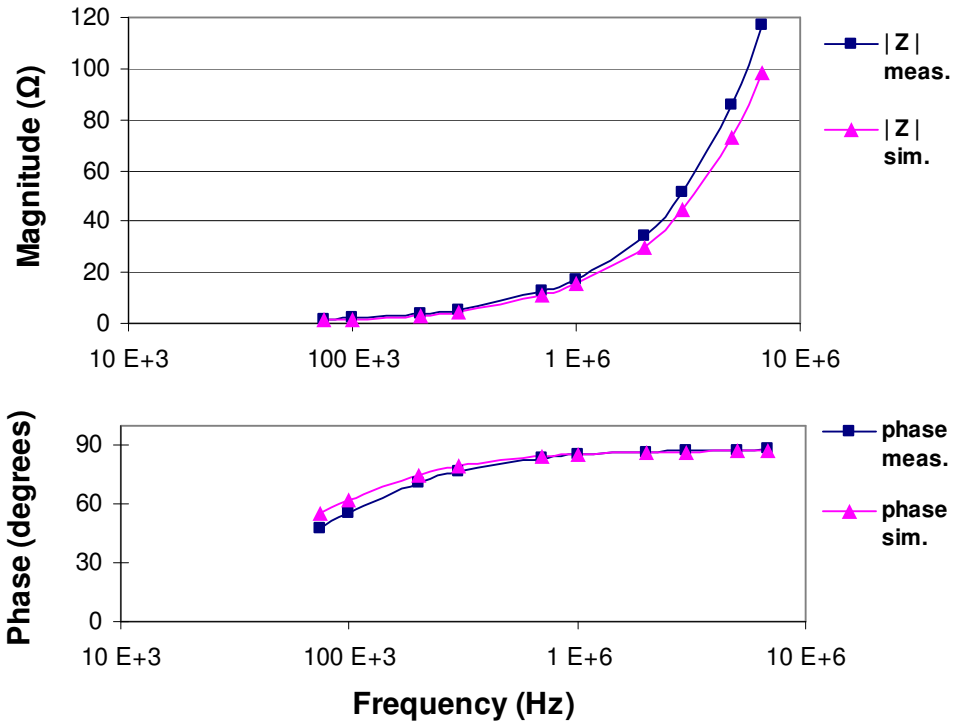


**Figure 8.4 Measured and simulated impedance for 100-turn polyethylene core solenoid**

## 8.3 Comparison of 2D and 3D Simulation

It is interesting to test the agreement between 2D and 3D simulations for mutual inductance. This was done by comparing the results of the simulation for a special case where both models represent an axisymmetric configuration of the coils where the secondary is parallel and centered with the primary. Table 8.2 shows this comparison where mutual inductance between a 14-turn primary and 50-turn ferrite-core secondary has been calculated.

**Table 8.2 Comparison of 2D and 3D Simulation of Mutual Inductance (H)**

| frequency (MHz) | 0.70 | | 0.30 | |
|---|---|---|---|---|
| | $M_{RE}$ | $M_{IM}$ | $M_{RE}$ | $M_{IM}$ |
| *COMSOL* 2D | 301.1 E-09 | 343.1 E-12 | 301.0 E-09 | 69.0 E-12 |
| *COMSOL* 3D | 287.1 E-09 | 325.0 E-12 | 287.0 E-09 | 61.6 E-12 |

Mutual inductance is a complex value in Table 8.2 due to the complex nature of the ferrite permeability, which was obtained from [108] for ferrite type 3C90. Since $\mu_r = \mu_r' - j\mu_r''$ then $M = M_{RE} - jM_{IM}$ where the real and imaginary parts are reported above. As seen from the table, there is good agreement between the 2D and 3D simulations for this simple geometrical configuration. However, the 3D simulation is more flexible as it can be used for off-axis positions and arbitrary orientations of the secondary coil relative to the primary coil.

## 8.4 Comparison of 3D Simulation to Calculation and Measurement of Mutual Inductance

The results of 3D simulation for the 14-turn primary and 50-turn ferrite-core secondary are shown in Figure 8.5. This is a plot of the magnitude (absolute value) of mutual inductance where the position and orientation of the secondary has been varied at three frequencies of interest. As described in section 7, beginning at the horizontal and vertical centre of the primary, the ferrite volume was moved radially outward to 2 cm and 4 cm, and vertically upward to 2.5 cm and 5 cm. Its angle was varied from parallel with the primary (0°) to 30° and 60° misalignments at each of these locations.

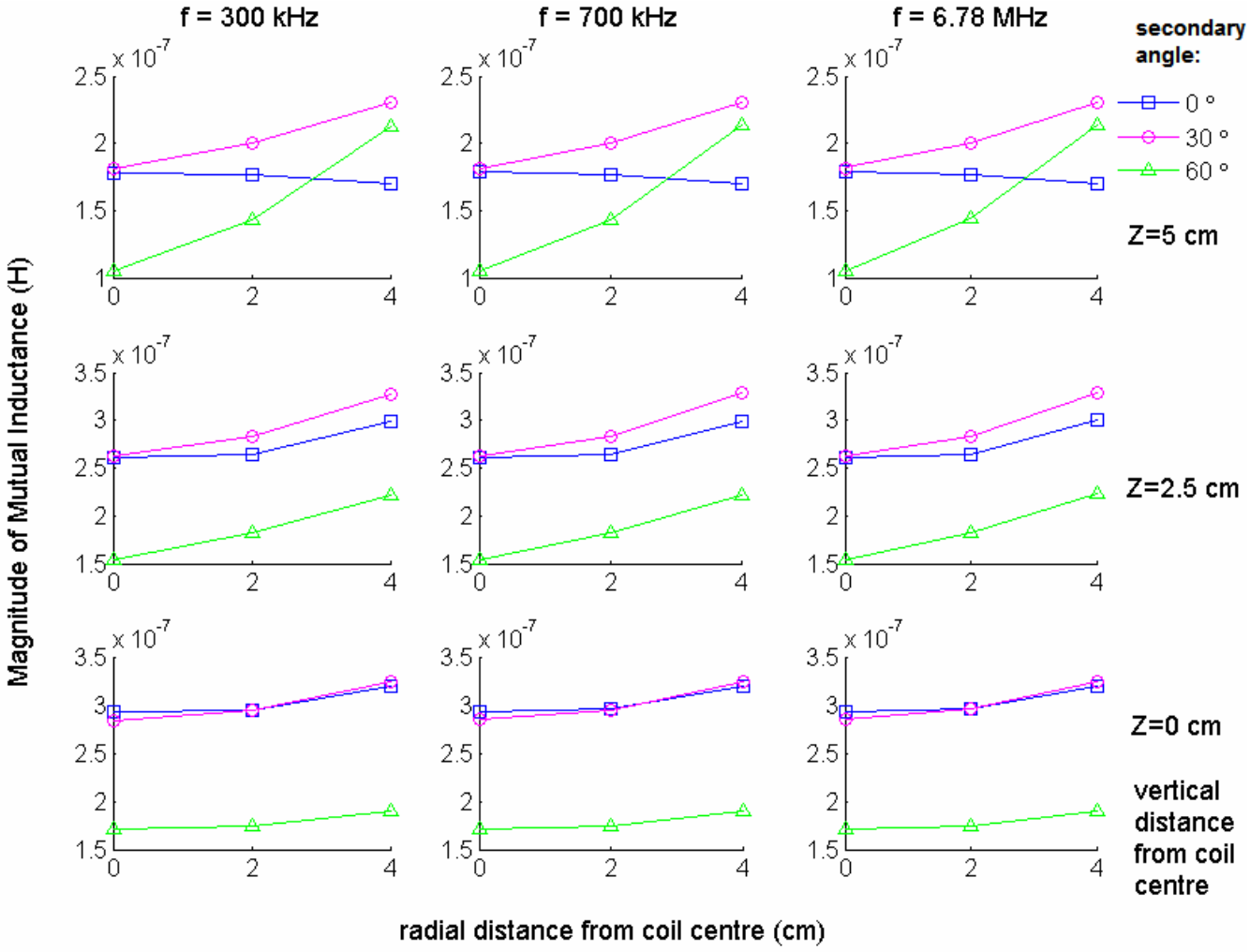


**Figure 8.5 Simulation of mutual inductance for various positions and orientations of the secondary coil at three frequencies**

To better understand the trends in Figure 8.5, a typical plot of the magnetic flux density surrounding the primary coil, as obtained from *COMSOL*, is shown in Figure 8.6.

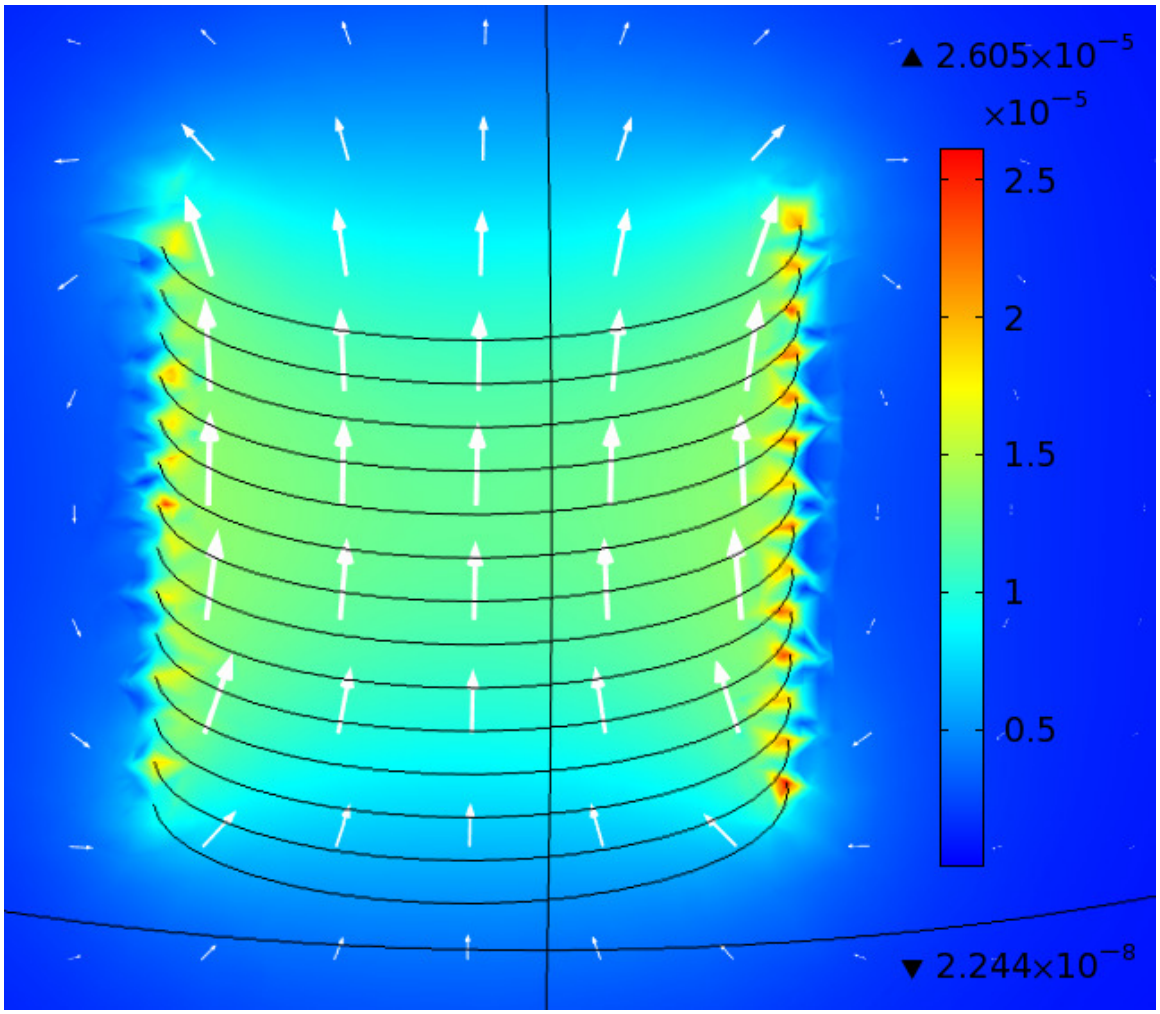


**Figure 8.6 Magnetic flux density norm (T) for 14-turn primary coil**

For comparison with the 3D simulation results of mutual inductance, values obtained from some commonly cited analytical formulas, as well as those obtained from experimental measurement of the coil voltages were computed and plotted in Figure 8.7 below. The formulas were introduced above in section 4.6, all values were calculated at 700 kHz.

In the left plot of Figure 8.7 the algorithm from [143] was used. This method assumes a uniform current distribution in the cross-section of the coils, and subdivides its length

and width to form rings. The mutual inductance between each ring of the primary and secondary coil is summed, producing the total between coils. The method was implemented in *MATLAB* in the present study; the script and functions are provided in Appendix E.

In the right plot, the mutual inductance is obtained from measured coil voltages as described in chapter 7.

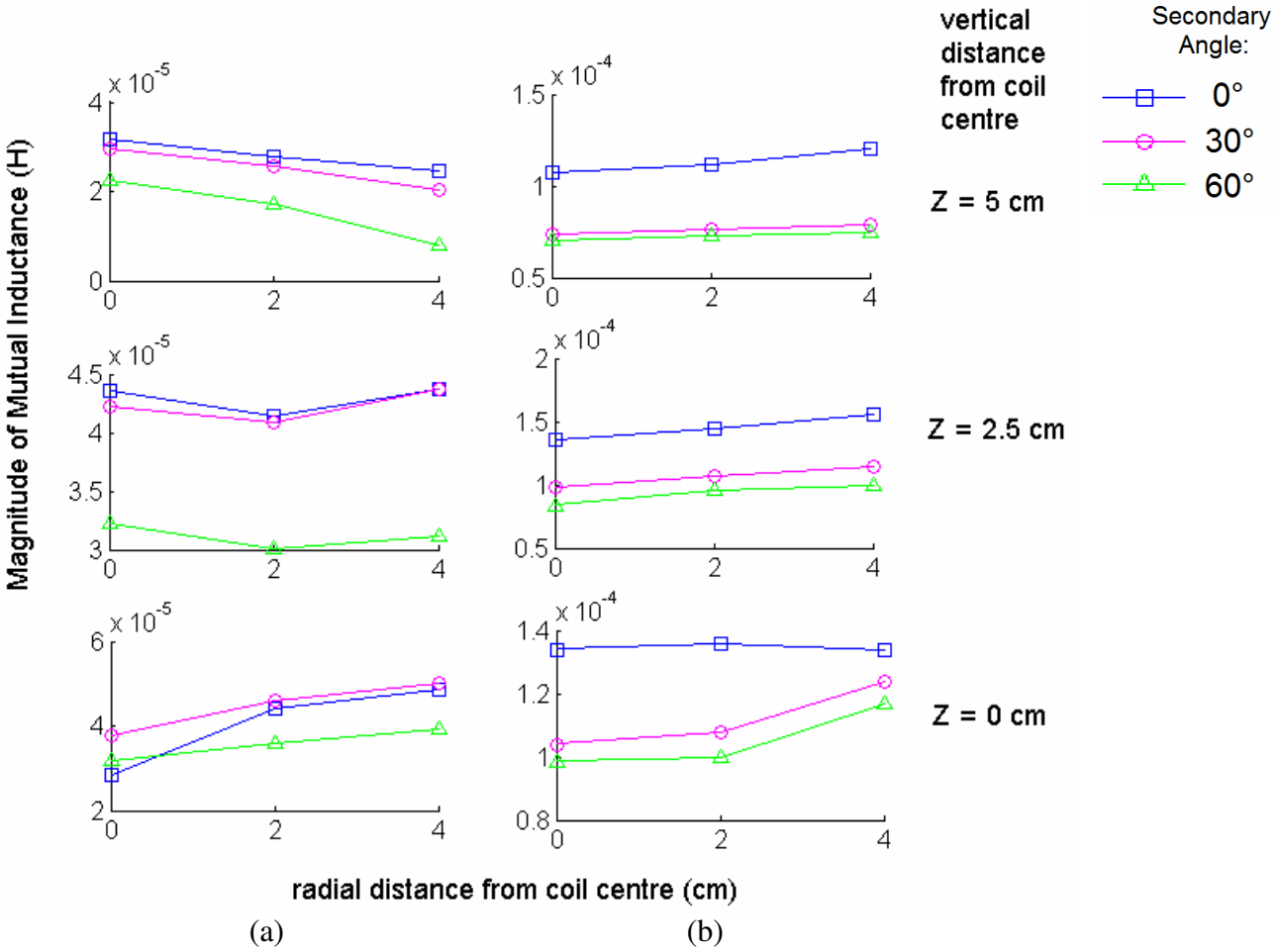


**Figure 8.7 Mutual inductance calculated by (a) analytical algorithm for coils with width and length, and (b) formula using measurement of coil voltages.**

Using $|M|$ from the 3D simulation (for the parallel, and centred secondary), and $R_2 = R_{ESR}$ from the 2D simulation, with an input current of 0.1 A applied to the primary, some values for power supplied to an example load of $R_L$ = 100 Ω are calculated in Table 8.3 using equation (8), with reference to the circuit of Figure 4.1.

**Table 8.3 Calculation of Maximum Power Dissipation (μW)**

| frequency (MHz) | 0.70 | 0.30 |
|---|---|---|
| $P_{R_L Max}$ for 50-turn ferrite core | 80.8 | 15.0 |
| $P_{R_L Max}$ for 100-turn ferrite core | 1300 | 239 |
| $P_{R_L Max}$ for 100-turn air core | 1.02 | 0.187 |

If the value of mutual inductance determined by experiment (measurement of coil voltages) is used instead in the calculation of power dissipation above, the result is much higher. For the same geometry, it is 1.46 W, which is more than three orders of magnitude greater than the largest value in Table 8.3.

The dissipation of energy in the coils due to ohmic heating could be calculated in a similar way as the power in the load, towards calculating the efficiency of the coupled coil circuit. This next step exceeds the scope of the present investigation.

## 8.5 Discussion

The calculated and simulated results show that for low frequencies (down to dc), FEM simulation produces nearly the same result as traditional analytically derived formulas for resistance and inductance of solenoid coils (see Table 8.1).

Referring to Figures 8.1 to 8.4 it is apparent that simulation is also an accurate method to obtain the equivalent resistance and inductance values for the series RL representation of a coil inductor, but only below the self-resonant frequency. (This result is satisfactory because the inductively coupled link is operated below the coil self-resonant frequency anyway). The simulated values are very close to the measurements in all cases except in Figure 8.2 at higher frequencies, where measurement reveals a self-resonance (impedance magnitude reaches maximum with corresponding phase change).

In Table 8.2, the simulated values for mutual inductance are in good agreement, and differ between the 2D and 3D models by about 4%, which is not unexpected considering they have differently sized elements and mesh, and the coils are represented by different physical domains. These results suggest that the simplification of representing the primary coil geometry with current specified on a path is justified.

Figure 8.5 shows nearly identical values for mutual inductance predicted by simulation over the three frequencies studied. For a coil with ferrite core, the mutual inductance is largely determined by the magnetic properties of the material. In the middle of the primary (away from the ends), mutual inductance increases slightly as the secondary is moved from the centre towards the windings of the primary. This is explained by higher flux density towards the windings as shown in Figure 8.6. The mutual inductance can be seen to decrease as the angular orientation of the secondary deviates from being parallel with the field generated by the primary. This is apparent from Figure 8.5, and is a result of less magnetic flux being captured by the turns of the secondary as the angle between it and the field direction increases.

Figure 8.7 compares the mutual inductance for various positions and angles of the secondary within the primary, as calculated by the algorithm described at the end of section 4.6, and by the results of experimental measurement using (26) from chapter 7. The results differ by up to an order of magnitude, where the analytically-developed algorithm produces smaller values than the measurement, although the general trends are noted to be similar. The voltage measured at the secondary is somewhat higher towards the circumference of the primary as compared to a secondary coil located coaxially. The analytically-developed algorithm is shown to produce values somewhere between those of simulation and measurement.

It is clear from Table 8.3 that the coil turns and core material have a dramatic effect on the coupling and hence the power dissipation in the load. The calculation of maximum power in this table specifies $C_2$ to ensure resonance, however as discussed above in section 4.4, maximum power transfer also requires the load resistance to match the resistive loss in the receiver coil. This is not the case for Table 8.3; the values reported are mostly in the microwatt level due to the difference between the chosen example load of 100 Ω and the secondary coil losses (ESR) that were simulated to be less than an ohm (see Table 8.1). The losses are expected to increase somewhat for an implanted circuit which would improve the load matching. Further, more power is transferred if the primary coil current is increased.

## 8.6 Summary

To summarize, it has been demonstrated that 2D FEM simulation is a very accurate method to model multi-turn solenoid coils for a frequency range extending from dc up to self-resonance.

It has also been shown that a simple 2D model is as effective as a 3D model for determining mutual inductance in the case where symmetry allows its use. However, the full 3D representation is generally necessary because an implanted sensor could be located at any radial distance from the long axis of the external coil, and may not be aligned with this axis either.

It has also been demonstrated that simulation results predict less mutual inductance than the analytical formula, which predicts less than that calculated from measurement.

# 9 Conclusion

## 9.1 Contributions

The implementation of an inductively coupled link to deliver wireless power to an implantable device requires consideration of many physical factors including the effects on the body, and how the body will affect the coupled circuit. These concepts have been introduced here with reference to the relevant literature.

Most significantly, a novel approach in predicting the degree of coupling between solenoid inductors has been presented in order to rapidly determine the power that may be wirelessly transferred to an implantable circuit.

A computational method (using FEM) was developed that allows the above calculations with two significant improvements over existing methods. These are the ability to consider

- 3D non-symmetrical coil arrangements, and the
- Use of magnetic material (ferrite-cores) in the secondary coil

## 9.2 Future Work

In the 3D simulation, the primary coil is modeled as a cylindrical helix, so that the simulations could be compared to previous analytical works. However, considering the proposed application for prosthesis use and referring to Figure 1.1, it can be seen that strictly cylindrical primary coils may not fit well within a prosthesis socket. Rather, the primary coil incorporated into a wearable device is likely somewhat conical and perhaps elliptical in cross-section. In this case, the use of a fully 3D FEM simulation becomes even more valuable for modeling of power transfer through inductive coupling.

A further change to the 3D FEM model to better represent the scenario of implanted devices in the upper limb would be to include an additional cylindrical volume to represent the residual portion of an adult or child sized arm. Although it would be very difficult to include all of the various tissue structures including skin, bone, fat, muscle and tendon, a first order approximation could be made by simply applying the properties of muscle in the limb volume; the permittivity of muscle tissue was measured in [79]. Also, multiple secondary coils could be positioned throughout this tissue volume to simulate their interaction.

Next, the secondary windings could be represented by defining a thin cylinder surrounding the magnetic core, with a thickness equal to a wire diameter, and specifying the properties of the copper conductor there.

The most significant improvement to the model would be to represent the primary coil not with a filamentary current path as done here, but with a fully three-dimensional helix. As mentioned above, this was attempted here at first but meshing of the structure was

problematic, and a solution to the model was not possible. It is anticipated that a computer with even more RAM could potentially accommodate the real geometry of both primary and secondary coils. Because the current would then be distributed over a finite space, a resistance is created, and a voltage could be applied or measured across the coil. The coils could be directly integrated with the lumped circuit model by connecting a *SPICE* representation with the *COMSOL* FEM software.

To further explore the relation between the simulation and formula for mutual inductance, a wider range of coil geometries, core materials and operating frequencies could be investigated. The core material in particular should be chosen according to the frequency requirements, which was not done here. Instead, the core choice here was motivated by the availability of ferrite with rod-shaped geometry.

Having established a flexible and rapid method for modelling the coils involved in a wireless power transfer system, the power transferred to a resistive load representing the power supplied to the implanted circuit has been calculated. With the modelling approach that has been described, the geometry of each coil as well as any core material properties may be varied as part of the design process. Multiple design iterations are likely required to obtain a final configuration that is typically optimized either for system-wide efficiency or insensitivity to coil coupling. Further detail on these topics is available in [9], [102], [104], [150].

The next step in the development of a complete EMG sensor system is the design of the external driving circuit as well as the implant electronics. The former is often implemented with a class E topology to maximize efficiency. The implant circuit typically includes a rectifier and voltage regulator. To detect muscle EMG, an

instrumentation amplifier with high input impedance could be employed. One strategy for back-telemetry of the muscle activity data is through load modulation of the secondary impedance. This effectively detunes the secondary in a controlled manner which is then detected at the primary side through an additional sensing coil.

## 9.3 Final Remarks

The possibility of enabling amputees to intuitively control advanced upper limb prostheses rests on the ability to detect a localized muscle activation signal. Implantable sensors have been proposed to do this, and the biological and electrical factors to be considered in their design have been presented here. A large part of modelling the wireless power transfer circuit is accurately representing the coupled inductor coils. The finite element method (FEM) has been applied here to simulate magnetic fields coupling the external transmitter and implanted receiver coils used in this wireless power transfer scheme. The validity of the computational method was confirmed by comparison to traditional analytic formulas for the self-inductance and ac resistance of wound inductors. In addition, physical prototypes of the simulated coils were measured, and these measurements produced results that were in good agreement with the computational results. Determination of these coil parameters is necessary for further calculation using the lumped circuit model or to calculate the coupling coefficient of the weakly coupled coils.

The use of FEM allows for flexible and rapid simulation of geometrical configurations and material properties with greater accuracy than analytical methods have allowed previously. The complex permeability of magnetic core material is easily incorporated

into the FEM model allowing its inclusion in the design process. Further, the three-dimensional nature of the simulation enables the calculation of power transfer at arbitrary orientations and positions between the implant and power source. In a more general sense, the proposed FEM approach becomes a potentially valuable tool for designing the next generation of implantable bio-sensors.

# Bibliography

[1] D. R. Merrill, J. Lockhart, P. R. Troyk, R. F. Weir, and D. L. Hankin, "Development of an Implantable Myoelectric Sensor for Advanced Prosthesis Control," *Artificial Organs*, 2011.

[2] T. D. Dissanayake et al., "A Novel Low Temperature Transcutaneous Energy Transfer System Suitable for High Power Implantable Medical Devices: Performance and Validation in Sheep," *Artificial Organs*, vol. 34, no. 5, p. E160–E167, 2010.

[3] S. Smith et al., "Development of a Miniaturised Drug Delivery System with Wireless Power Transfer and Communication," *IET Nanobiotechnology / IET*, vol. 1, no. 5, pp. 80-86, Oct. 2007.

[4] J. C. Schuder, "Powering an artificial heart: Birth of the inductively coupled-radio frequency system in 1960," *Artificial organs*, vol. 26, no. 11, pp. 909–915, 2002.

[5] R. Arzbaecher, D. R. Hampton, M. C. Burke, and M. C. Garrett, "Subcutaneous Electrocardiogram Monitors and Their Field of View," *Journal of Electrocardiology*, vol. 43, no. 6, pp. 601-605, 2010.

[6] J. H. Schulman, "The Feasible FES System: Battery Powered BION Stimulator," *Proceedings of the IEEE*, vol. 96, no. 7, pp. 1226-1239, Jul. 2008.

[7] K. D. Wise, D. J. Anderson, J. F. Hetke, D. R. Kipke, and K. Najafi, "Wireless Implantable Microsystems: High-Density Electronic Interfaces to the Nervous System," *Proceedings of the IEEE*, vol. 92, no. 1, pp. 76-97, Jan. 2004.

[8] C. K. Liang, J. J. J. Chen, C. L. Chung, C. L. Cheng, and C. C. Wang, "An Implantable Bi-Directional Wireless Transmission System for Transcutaneous Biological Signal Recording," *Physiological Measurement*, vol. 26, p. 83, 2005.

[9] B. Lenaerts and R. Puers, *Omnidirectional Inductive Powering for Biomedical Implants*. Dordrecht: Springer Netherlands, 2009.

[10] H. A. Ghali and H. A. Rahman, "Understanding 'Mutual Inductance' using COMSOL Multiphysics," in *Proceedings of the Comsol Conference*, Milan, 2009.

[11] E. A. Biddiss and T. T. Chau, "Upper Limb Prosthesis Use and Abandonment: A Survey of the Last 25 Years," *Prosthetics and Orthotics International*, vol. 31, no. 3, pp. 236-257, Jan. 2007.

[12] "The i-LIMB Hand," *Touch Bionics. Hilliard, OH*, 2011. [Online]. Available: http://www.touchbionics.com/i-LIMB.

[13] P. J. Kyberd, C. Light, P. H. Chappell, J. M. Nightingale, D. Whatley, and M. Evans, "The Design of Anthropomorphic Prosthetic Hands: A Study of the Southampton Hand," *Robotica*, vol. 19, no. 6, pp. 593–600, 2001.

[14] "Utah Arm," *Motion Control, Inc. Salt Lake City, UT*, 2011. [Online]. Available: http://www.utaharm.com/.

[15] J. Davidson, "A Survey of the Satisfaction of Upper Limb Amputees with Their Prostheses, Their Lifestyles, and Their Abilities," *Journal of Hand Therapy*, vol. 15, no. 1, pp. 62–70, 2002.

[16] D. J. Atkins, D. C. Y. Heard, and W. H. Donovan, "Epidemiologic Overview of Individuals with Upper-Limb Loss and Their Reported Research Priorities," *Journal of Prosthetics and Orthotics*, vol. 8, no. 1, pp. 2-11, 1996.

[17] R. A. Prokopenko, A. A. Frolov, E. V. Biryukova, and A. Roby-Brami, "Assessment of the accuracy of a human arm model with seven degrees of freedom," *Journal of Biomechanics*, vol. 34, no. 2, pp. 177-185, Feb. 2001.

[18] S. Adee, "The Revolution Will Be Prosthetized," *IEEE Spectrum*, Jan. 2009.

[19] M. C. Carrozza et al., "The Spring Hand: Development of a Self-Adaptive Prosthesis for Restoring Natural Grasping," *Autonomous Robots*, vol. 16, no. 2, pp. 125–141, 2004.

[20] M. Controzzi, C. Cipriani, B. Jehenne, M. Donati, and M. C. Carrozza, "Bio-Inspired Mechanical Design of a Tendon-Driven Dexterous Prosthetic Hand," in *32nd Annual International Conference IEEE Engineering in Medicine and Biology Society*, Buenos Aires, Argentina, 2010, pp. 499–502.

[21] N. Dechev, W. L. Cleghorn, and S. Naumann, "Multiple Finger, Passive Adaptive Grasp Prosthetic Hand," *Mechanism and Machine Theory*, vol. 36, no. 10, pp. 1157–1173, 2001.

[22] S. Jacobsen, E. Iversen, D. Knutti, R. Johnson, and K. Biggers, "Design of the Utah/MIT Dextrous Hand," in *Proceedings of 1986 IEEE International Conference on Robotics and Automation*, vol. 3, pp. 1520–1532.

[23] C. M. Light and P. H. Chappell, "Development of a Lightweight and Adaptable Multiple-Axis Hand Prosthesis," *Medical Engineering & Physics*, vol. 22, no. 10, pp. 679-684, Dec. 2000.

[24] P. Tuffield and H. Elias, "The Shadow robot mimics human actions," *Industrial Robot: An International Journal*, vol. 30, no. 1, pp. 56-60, 2003.

[25] J. Yang, E. P. Pitarch, K. Abdel-Malek, A. Patrick, and L. Lindkvist, "A Multi-Fingered Hand Prosthesis," *Mechanism and Machine Theory*, vol. 39, no. 6, pp. 555–581, 2004.

[26] T. A. Kuiken et al., "Targeted Muscle Reinnervation for Real-Time Myoelectric Control of Multifunction Artificial Arms," *Journal of the American Medical Association*, vol. 301, no. 6, pp. 619-628, Feb. 2009.

[27] G. A. DeMichele, P. R. Troyk, D. A. Kerns, and R. Weir, "An Implantable Myoelectric Sensor Based Prosthesis Control System," in *Proceedings of 28th Annual International Conference of the IEEE Engineering in Medicine and Biology Society*, 2006, vol. 1, pp. 2970-2973.

[28] R. F. Weir, P. R. Troyk, G. A. DeMichele, D. A. Kerns, J. F. Schorsch, and H. Maas, "Implantable Myoelectric Sensors (IMESs) for Intramuscular Electromyogram Recording," *IEEE Transactions on Biomedical Engineering*, vol. 56, no. 1, pp. 159-171, 2009.

[29] B. D. Farnsworth, R. J. Triolo, and D. J. Young, "Wireless Implantable EMG Sensing Microsystem," *IEEE Sensors Journal*, pp. 1245–1248, 2008.

[30] R. Merletti and P. Parker, Eds., *Electromyography: Physiology, Engineering, and Noninvasive Applications*. Wiley-IEEE Press, 2004.

[31] T. F. Weiss, *Cellular Biophysics, Vol. 2: Electrical Properties*. The MIT Press, 1996.

[32] Z. O. Khokhar, Z. G. Xiao, and C. Menon, "Surface EMG Pattern Recognition for Real-Time Control of a Wrist Exoskeleton," *BioMedical Engineering OnLine*, vol. 9, no. 1, p. 41, 2010.

[33] T. R. Farrell and R. Weir, "A Comparison of the Effects of Electrode Implantation and Targeting on Pattern Classification Accuracy for Prosthesis Control," *IEEE Transactions on Biomedical Engineering*, vol. 55, no. 9, pp. 2198-2211, Sep. 2008.

[34] L. J. Hargrove, K. Englehart, and B. Hudgins, "A Comparison of Surface and Intramuscular Myoelectric Signal Classification," *IEEE Transactions on Biomedical Engineering*, vol. 54, no. 5, pp. 847-853, May. 2007.

[35] K. Englehart and B. Hudgins, "A Robust, Real-Time Control Scheme for Multifunction Myoelectric Control," *IEEE Transactions on Biomedical Engineering*, vol. 50, no. 7, pp. 848-854, Jul. 2003.

[36] A. B. Ajiboye, R. F. Weir, C. W. Heckathorne, and D. S. Childress, "Neurofuzzy Logic as a Control Algorithm for an Externally Powered Multifunctional Hand Prosthesis," in *Proc. 2002 MyoElectric Controls/Powered Prosthetics Symposium*, Fredericton, New Brunswick, Canada, 2002.

[37] F. Tenore, A. Ramos, A. Fahmy, S. Acharya, R. Etienne-Cummings, and N. V. Thakor, "Towards the Control of Individual Fingers of a Prosthetic Hand Using Surface EMG Signals," in *29th Annual International Conference of the IEEE Engineering in Medicine and Biology Society*, 2007, pp. 6145-6148.

[38] A. B. Ajiboye and R. F. H. Weir, "A Heuristic Fuzzy Logic Approach to EMG Pattern Recognition for Multifunctional Prosthesis Control," *IEEE Transactions on Neural Systems and Rehabilitation Engineering*, vol. 13, no. 3, pp. 280-291, Sep. 2005.

[39] J. J. Baker, E. Scheme, K. Englehart, D. T. Hutchinson, and B. Greger, "Continuous Detection and Decoding of Dexterous Finger Flexions With Implantable MyoElectric Sensors," *IEEE Transactions on Neural Systems and Rehabilitation Engineering*, vol. 18, no. 4, pp. 424-432, Aug. 2010.

[40] C. Castellini and P. Smagt, "Surface EMG in Advanced Hand Prosthetics," *Biological Cybernetics*, vol. 100, no. 1, pp. 35-47, Nov. 2008.

[41] K. Englehart, B. Hudgin, and P. A. Parker, "A Wavelet-Based Continuous Classification Scheme for Multifunction Myoelectric Control," *IEEE Transactions on Biomedical Engineering*, vol. 48, no. 3, pp. 302-311, Mar. 2001.

[42] M. Asghari Oskoei and H. Hu, "Myoelectric control systems–A survey," *Biomedical Signal Processing and Control*, vol. 2, no. 4, pp. 275–294, 2007.

[43] M. Kawato, "Internal models for motor control and trajectory planning," *Current Opinion in Neurobiology*, vol. 9, no. 6, pp. 718–727, 1999.

[44] N. Bhushan and R. Shadmehr, "Evidence for a Forward Dynamics Model in Human Adaptive Motor Control," in *Advances in Neural Information Processing Systems*, vol. 11, Cambridge MA: MIT Press, 1999, pp. 3-9.

[45] A. Isidori, L. Marconi, and A. Serrani, *Robust Autonomous Guidance: An Internal Model Approach*, 1st ed. Springer, 2003.

[46] W. Tsang, K. Singh, and E. Fiume, "Helping hand: an anatomically accurate inverse dynamics solution for unconstrained hand motion," in *Proceedings of the 2005 ACM SIGGRAPH/Eurographics Symposium on Computer Animation*, 2005, pp. 319–328.

[47] J. Rosen, M. Brand, M. B. Fuchs, and M. Arcan, "A Myosignal-Based Powered Exoskeleton System," *IEEE Transactions on Systems, Man and Cybernetics, Part A: Systems and Humans*, vol. 31, no. 3, pp. 210–222, 2001.

[48] J. Perry, C. S. Easterday, and D. J. Antonelli, "Surface Versus Intramuscular Electrodes for Electromyography of Superficial and Deep Muscles," *Physical Therapy*, vol. 61, no. 1, p. 7, 1981.

[49] R. Vinjamuri, Zhi-Hong Mao, R. Sclabassi, and Mingui Sun, "Limitations of Surface EMG Signals of Extrinsic Muscles in Predicting Postures of Human Hand," in *Proceedings of 28th Annual International Conference of the IEEE Engineering in Medicine and Biology Society*, New York City, NY, 2006, pp. 5491-5494.

[50] J. V. Basmajian, *Muscles Alive: Their Functions Revealed by Electromyography*, 4th ed. Williams & Wilkins, 1979.

[51] "Cross-Section Through the Middle of the Forearm (Gray's Anatomy Fig. 417)," *Wikimedia Commons*. [Online]. Available: http://en.wikipedia.org/wiki/File:Gray417_color.PNG.

[52] "SEER Training: Structure of Skeletal Muscle," *Cancer.gov*. [Online]. Available: http://training.seer.cancer.gov/anatomy/muscular/structure.html.

[53] J. Chae, J. Knutson, R. Hart, and Z. P. Fang, "Selectivity and Sensitivity of Intramuscular and Transcutaneous Electromyography Electrodes," *American Journal of Physical Medicine & Rehabilitation*, vol. 80, no. 5, p. 374, 2001.

[54] R. F. Weir, P. R. Troyk, G. A. DeMichele, and D. Kerns, "Technical Details of the IMES System for Multifunction Prosthesis Control," in *Proceedings of the 27th Annual International Conference of the IEEE Engineering in Medicine and Biology Society*, Shanghai, China, 2005, pp. 7337-7340.

[55] P. R. Troyk, G. A. DeMichele, D. A. Kerns, and R. F. Weir, "IMES: An Implantable Myoelectric Sensor," in *Proceedings of 29th Annual International Conference of the IEEE Engineering in Medicine and Biology Society*, 2007, pp. 1730–1733.

[56] G. A. DeMichele, P. R. Troyk, D. Kerns, and R. F. Weir, "IMES - Implantable Myoelectric Sensor System: Designing Standardized ASICs," in *Proceedings of the IEEE Biomedical Circuits and Systems Conference*, 2008, pp. 117–120.

[57] R. F. Weir, P. R. Troyk, G. DeMichele, and T. Kuiken, "Implantable myoelectric sensors (IMES) for upper-extremity prosthesis control-preliminary work," in *Proceedings of the 25th Annual International Conference of the IEEE Engineering in Medicine and Biology Society*, 2003, vol. 2.

[58] J. F. Schorsch, R. F. Weir, and H. Maas, "Evaluation of Cross Talk Between Adjacent Muscles in Feline EMG Recorded Using Implantable MyoElectric Sensors (IMES)," in *Proceedings of the 18th Congress of the International Society of Electrophysiology & Kinesiology (ISEK)*, Aalborg, Denmark, 2010.

[59] M. M. Lowery, R. F. Weir, and T. A. Kuiken, "Simulation of Intramuscular EMG Signals Detected Using Implantable Myoelectric Sensors (IMES)," *IEEE Transactions on Biomedical Engineering*, vol. 53, no. 10, pp. 1926-1933, Oct. 2006.

[60] G. E. Loeb, R. A. Peck, W. H. Moore, and K. Hood, "BION System for Distributed Neural Prosthetic Interfaces," *Medical Engineering & Physics*, vol. 23, no. 1, pp. 9–18, 2001.

[61] P. R. Troyk, I. E. Brown, W. H. Moore, and G. E. Loeb, "Development of BION Technology for Functional Electrical Stimulation: Bidirectional Telemetry," in *Proceedings of 23rd Annual International Conference of the IEEE Engineering in Medicine and Biology Society*, 2001.

[62] G. E. Loeb, C. J. Zamin, J. H. Schulman, and P. R. Troyk, "Injectable Microstimulator for Functional Electrical Stimulation," *Medical & Biological Engineering & Computing*, vol. 29, no. 6, p. NS13-NS19, Nov. 1991.

[63] I. Arcos et al., "Second-Generation Microstimulator," *Artificial Organs*, vol. 26, no. 3, pp. 228–231, 2002.

[64] T. Cameron, T. L. Liinamaa, G. E. Loeb, and F. J. R. Richmond, "Long-Term Biocompatibility of a Miniature Stimulator Implanted in Feline Hind Limb Muscles," *IEEE Transactions on Biomedical Engineering*, vol. 45, no. 8, pp. 1024-1035, Aug. 1998.

[65] K. Roeleveld, J. H. Blok, D. F. Stegeman, and A. van Oosterom, "Volume conduction models for surface EMG; confrontation with measurements," *Journal of Electromyography and Kinesiology*, vol. 7, no. 4, pp. 221-232, Dec. 1997.

[66] M. Lowery, N. Stoykov, A. Taflove, and T. Kuiken, "A multi-layer finite element model of the surface EMG signal," in *Proceedings of the 23rd Annual International Conference of the IEEE Engineering in Medicine and Biology Society*, 2001, vol. 2, pp. 1051- 1054 vol.2.

[67] S. F. Cleary, "Cellular Effects of Electromagnetic Radiation," *Engineering in Medicine and Biology Magazine, IEEE*, vol. 6, no. 1, pp. 26-30, 1987.

[68] R. J. Smialowicz, "Immunologic Effects of Nonionizing Electromagnetic Radiation," *IEEE Engineering in Medicine and Biology Magazine*, vol. 6, no. 1, pp. 47-51, 1987.

[69] *Exposure to High Frequency Electromagnetic Fields, Biological Effects and Health Consequences (100 Khz-300 Ghz) - Review of the Scientific Evidence and Health Consequences*. Munich: International Commission on Non-Ionizing Radiation Protection, 2009.

[70] *IEEE Standard for Safety Levels With Respect to Human Exposure to Radio Frequency Electromagnetic Fields, 3 kHz to 300 GHz*. IEEE International Committee on Electromagnetic Safety (SCC39), 2006.

[71] ICNIRP, "Guidelines for Limiting Exposure to Time-Varying Electric, Magnetic, and Electromagnetic Fields (up to 300 GHz)," *Health Physics*, vol. 74, no. 4, pp. 494-522, 1998.

[72] C. Mattiussi, "The Finite Volume, Finite Element, and Finite Difference Methods as Numerical Methods for Physical Field Problems," *Journal of Computational Physics*, vol. 133, p. 289--309, 2000.

[73] R. P. Findlay and P. J. Dimbylow, "FDTD calculations of specific energy absorption rate in a seated voxel model of the human body from 10 MHz to 3 GHz," *Physics in Medicine and Biology*, vol. 51, no. 9, pp. 2339-2352, May. 2006.

[74] P. J. Dimbylow, "Fine resolution calculations of SAR in the human body for frequencies up to 3 GHz," *Physics in Medicine and Biology*, vol. 47, no. 16, pp. 2835-2846, Aug. 2002.

[75] P. Dimbylow, "Resonance Behaviour of Whole-Body Averaged Specific Energy Absorption Rate (sar) in the Female Voxel Model, Naomi," *Physics in Medicine and Biology*, vol. 50, no. 17, pp. 4053-4063, Sep. 2005.

[76] C. H. Durney, M. F. Iskander, H. Massoudi, and C. C. Johnson, "An Empirical Formula for Broad-Band SAR Calculations of Prolate Spheroidal Models of Humans and Animals," *IEEE Transactions on Microwave Theory and Techniques*, vol. 27, no. 8, pp. 758-763, 1979.

[77] W. J. Heetderks, "RF Powering of Millimeter-and Submillimeter-Sized Neural Prosthetic Implants," *IEEE Transactions on Biomedical Engineering*, vol. 35, no. 5, pp. 323–327, 1988.

[78] C. Gabriel, S. Gabriel, and E. Corthout, "The Dielectric Properties of Biological Tissues: I. Literature Survey," *Physics in Medicine and Biology*, vol. 41, no. 11, pp. 2231-2249, Nov. 1996.

[79] S. Gabriel, R. W. Lau, and C. Gabriel, "The Dielectric Properties of Biological Tissues: II. Measurements in the Frequency Range 10 Hz to 20 Ghz," *Physics in Medicine and Biology*, vol. 41, no. 11, pp. 2251-2269, Nov. 1996.

[80] A. S. Y. Poon, S. O'Driscoll, and T. H. Meng, "Optimal Frequency for Wireless Power Transmission Into Dispersive Tissue," *IEEE Transactions on Antennas and Propagation*, vol. 58, pp. 1739–1750, 2010.

[81] C. G. Montgomery, R. H. Dicke, and E. M. Purcell, *Principles of Microwave Circuits*. IET, 1987.

[82] I. J. Bahl, *Lumped Elements for RF and Microwave Circuits*. Artech House, 2003.

[83] M. Catrysse, B. Hermans, and R. Puers, "An Inductive Power System with Integrated Bi-Directional Data-Transmission," *Sensors and Actuators A: Physical*, vol. 115, no. 2-3, pp. 221-229, Sep. 2004.

[84] G. Vandevoorde and R. Puers, "Wireless Energy Transfer for Stand-Alone Systems: A Comparison Between Low and High Power Applicability," *Sensors and Actuators A: Physical*, vol. 92, no. 1-3, pp. 305–311, 2001.

[85] H. M. Lu, C. Goldsmith, L. Cauller, and J.-B. Lee, "MEMS-Based Inductively Coupled RFID Transponder for Implantable Wireless Sensor Applications," *IEEE Transactions on Magnetics*, vol. 43, no. 6, pp. 2412-2414, Jun. 2007.

[86] K. Finkenzeller, *RFID Handbook: Fundamentals and Applications in Contactless Smart Cards and Identification*, 3rd ed. Wiley, 2010.

[87] Y. Lee, *Antenna Circuit Design for RFID Applications*. Microchip Technologies, 2003.

[88] P. R. Troyk and S. F. Cogan, "Sensory Neural Prostheses," in *Neural Engineering*, Kluwer Academic, 2005, pp. 21–35.

[89] B. Lenaerts and R. Puers, "An Inductive Power Link for a Wireless Endoscope," *Biosensors and Bioelectronics*, vol. 22, no. 7, pp. 1390–1395, 2007.

[90] D. C. Ng, S. Bai, J. Yang, N. Tran, and E. Skafidas, "Wireless Technologies for Closed-Loop Retinal Prostheses," *Journal of Neural Engineering*, vol. 6, no. 6, p. 065004, Dec. 2009.

[91] C. M. Zierhofer and E. S. Hochmair, "Geometric approach for coupling enhancement of magnetically coupled coils," *IEEE Transactions on Biomedical Engineering*, vol. 43, no. 7, pp. 708-714, Jul. 1996.

[92] K. Fotopoulou and B. W. Flynn, "Optimum Antenna Coil Structure for Inductive Powering of Passive RFID Tags," in *IEEE International Conference on RFID*, 2007, pp. 71–77.

[93] W. H. Ko, S. P. Liang, and C. D. F. Fung, "Design of Radio-Frequency Powered Coils for Implant Instruments," *Medical and Biological Engineering and Computing*, vol. 15, no. 6, pp. 634–640, 1977.

[94] E. S. Hochmair, "System Optimization for Improved Accuracy in Transcutaneous Signal and Power Transmission," *IEEE Transactions on Biomedical Engineering*, vol. 31, no. 2, pp. 177-186, 1984.

[95] D. C. Galbraith, M. Soma, R. L. White, and I. Actel, "A Wide-Band Efficient Inductive Transdermal Power and Data Link with Coupling Insensitive Gain," *IEEE Transactions on Biomedical Engineering*, pp. 265–275, 1987.

[96] P. A. Neukomm and D. Furrer, "Design Rules for a Weakly Coupled Inductive Link avoiding the 'Black Hole' in Passive Telemetry Data Transmission for an Implantable Thermal Flow Sensor," in *Proceedings of the 17th Conference of the International Society on Biotelemetry*, Brisbane, 2003.

[97] G. A. Kendir et al., "An Optimal Design Methodology for Inductive Power Link with Class-E Amplifier," *IEEE Transactions on Circuits and Systems I: Regular Papers*, vol. 52, no. 5, pp. 857-866, May. 2005.

[98] R. Puers, K. Schuylenbergh, M. Catrysse, and B. Hermans, "Wireless Inductive Transfer of Power and Data," in *Analog Circuit Design*, Springer Science & Business, 2006, pp. 395–414.

[99] P. Si et al., "Wireless Power Supply for Implantable Biomedical Device Based on Primary Input Voltage Regulation," in *2nd IEEE Conference on Industrial Electronics and Applications*, 2007, pp. 235–239.

[100] M. Ghovanloo and S. Atluri, "A Wide-Band Power-Efficient Inductive Wireless Link for Implantable Microelectronic Devices Using Multiple Carriers," *IEEE Transactions on Circuits and Systems I: Regular Papers*, vol. 54, no. 10, pp. 2211-2221, Oct. 2007.

[101] M. Guanying, Y. Guozheng, and H. Xiu, "Power Transmission for Gastrointestinal Microsystems Using Inductive Coupling," *Physiological Measurement*, vol. 28, no. 3, p. N9-N18, Mar. 2007.

[102] J. Sacristán-Riquelme, F. Segura, and M. T. Osés, "Simple and Efficient Inductive Telemetry System with Data and Power Transmission," *Microelectronics Journal*, vol. 39, no. 1, pp. 103–111, 2008.

[103] Q. Chen, S. C. Wong, C. K. Tse, and X. Ruan, "Analysis, Design, and Control of a Transcutaneous Power Regulator for Artificial Hearts," *IEEE Transactions on Biomedical Circuits and Systems*, vol. 3, no. 1, pp. 23-31, Feb. 2009.

[104] K. van Schuylenbergh and R. Puers, *Inductive Powering: Basic Theory and Application to Biomedical Systems*, 1st ed. Springer Science & Business, 2009.

[105] F. E. Terman, *Radio Engineer's Handbook*. NY: McGraw-Hill Book Company, Inc., 1943.

[106] W. Hayt, *Engineering Electromagnetics*, 6th ed. McGraw-Hill Inc., 2001.

[107] E. C. Snelling, "Chapter 8 - Magnetic Materials," in *Electrical Engineer's Reference Book*, 16th ed., M. A. Laughton and D. F. Warne, Eds. Elsevier, 2003.

[108] "Soft Ferrites and Accessories Data Handbook," *Ferroxcube*, 2009. [Online]. Available: http://www.ferroxcube.com/appl/info/HB2009.htm.

[109] P. T. Theilmann and P. M. Asbeck, "An Analytical Model for Inductively Coupled Implantable Biomedical Devices With Ferrite Rods," *IEEE Transactions on Biomedical Circuits and Systems*, vol. 3, no. 1, pp. 43-52, Feb. 2009.

[110] M. Soma, D. C. Galbraith, and R. L. White, "Radio-Frequency Coils in Implantable Devices: Misalignment Analysis and Design Procedure," *IEEE Transactions on Biomedical Engineering*, pp. 276–282, 1987.

[111] R. M. Bozorth, "Demagnetizing Factors of Rods," *Journal of Applied Physics*, vol. 13, no. 5, p. 320, 1942.

[112] D. C. Yates, A. S. Holmes, and A. J. Burdett, "Optimal Transmission Frequency for Ultralow-Power Short-Range Radio Links," *IEEE Transactions on Circuits and Systems I: Regular Papers*, vol. 51, no. 7, pp. 1405-1413, Jul. 2004.

[113] K. Sylvan, J. R. Jordan, and H. W. Whittington, "A Shunt-Excited Inductive Power Link," *Journal of Medical Engineering & Technology*, vol. 13, no. 4, pp. 215–219, 1989.

[114] *Agilent Impedance Measurement Handbook 4th Ed.* Agilent Technologies, 2009.

[115] W. B. Kuhn and A. P. Boutz, "Measuring and Reporting High Quality Factors of Inductors Using Vector Network Analyzers," *IEEE Transactions on Microwave Theory and Techniques*, vol. 58, no. 4, pp. 1046-1055, Apr. 2010.

[116] D. Kajfez, S. Chebolu, M. R. Abdul-Gaffoor, and A. A. Kishk, "Uncertainty Analysis of the Transmission-Type Measurement of Q-Factor," *IEEE Transactions on Microwave Theory and Techniques*, vol. 47, no. 3, pp. 367-371, 1999.

[117] D. Kleijer, "Measuring the Q of LC circuits," *crystal-radio.eu*. [Online]. Available: http://www.crystal-radio.eu/enqmeting.htm. [Accessed: 05-Jul-2011].

[118] J. C. Maxwell, *A Treatise on Electricity and Magnetism*, vol. 2. 1873.

[119] D. W. Knight, "The Self-Resonance and Self-Capacitance of Solenoid Coils," *G3YNH.info*, 09-May-2010. [Online]. Available: http://www.g3ynh.info/zdocs/magnetics/appendix/self-res.html. [Accessed: 24-May-2011].

[120] M. C. Thompson, "Inductance Calculation Techniques - Part I: Classical Methods," *Power Control and Intelligent Motion*, pp. 40-45, Dec-1999.

[121] H. A. Wheeler, "Simple Inductance Formulas for Radio Coils," *Proceedings of the Institute of Radio Engineers*, vol. 16, no. 10, pp. 1398–1400, 1928.

[122] H. A. Wheeler, "Discussion on Simple Inductance Formulas for Radio Coils," *Proceedings of the Institute of Radio Engineers*, vol. 17, no. 3, pp. 580-582, 1929.

[123] H. A. Wheeler, "Inductance Formulas for Circular and Square Coils," *Proceedings of the IEEE*, vol. 70, no. 12, pp. 1449–1450, 1982.

[124] F. W. Grover, *Inductance Calculations: Working Formulas and Tables*. Courier Dover Publications, 2004.

[125] F. W. Grover, "Additions to the Formulas for the Calculation of Mutual and Self Inductance," *Bulletin of the Bureau of Standards*, vol. 14, no. 4, pp. 537-570, Jul. 1919.

[126] E. B. Rosa and F. W. Grover, "Formulas and Tables for the Calculation of Mutual and Self Inductance," *Bulletin of the Bureau of Standards No. 169*, vol. 8, no. 1, Dec. 1916.

[127] M. C. Thompson, "Inductance Calculation Techniques - Part II: Approximations and Handbook Methods," *Power Control and Intelligent Motion*, Dec-1999.

[128] K. L. Corum, P. V. Pesavento, and J. F. Corum, "Multiple Resonances in RF Coils and the Failure of Lumped Inductance Models," presented at the Sixth International Symposium Nikola Tesla, Belgrade, Serbia, 2006.

[129] K. L. Corum and J. F. Corum, "RF Coils, Helical Resonators and Voltage Magnification by Coherent Spatial Modes," *Microwave Review*, pp. 36-45, Sep. 2001.

[130] R. G. Medhurst, "H. F. Resistance and Self-Capacitance of Single-Layer Solenoids," *Wireless Engineer*, pp. 35-43 Feb. 1947 pp. 80-92, Mar-1947.

[131] H. A. Wheeler, "Formulas for the Skin Effect," *Proceedings of the Institute of Radio Engineers*, vol. 30, no. 9, pp. 412–424, 1942.

[132] D. W. Knight, "Practical Continuous Functions for the Internal Impedance of Solid Cylindrical Conductors," *G3YNH.info*, 19-Oct-2010. [Online]. Available: http://www.g3ynh.info/zdocs/comps/zint/index.html.

[133] E. Fraga, C. Prados, and D. X. Chen, "Practical Model and Calculation of AC Resistance of Long Solenoids," *IEEE Transactions on Magnetics*, vol. 34, no. 1, pp. 205–212, 1998.

[134] H. B. Dwight, "Skin Effect in Tubular and Flat Conductors," *Transactions of the American Institute of Electrical Engineers*, vol. 37, no. 2, pp. 1379–1403, 1918.

[135] S. Ramo, J. R. Whinnery, and T. V. Duzer, *Fields and Waves in Communication Electronics*, 3rd ed. John Wiley & Sons, Inc., 1994.

[136] R. H. Good, "Elliptic Integrals, the Forgotten Functions," *European Journal of Physics*, vol. 22, p. 119, 2001.

[137] S. F. Pichorim and P. J. Abatti, "Design of Circular and Solenoid Coils for Maximum Mutual Inductance," in *Proceedings of the 14th International Symposium on Biotelemetry*, Marburg, Germany, 1997, pp. 71-76.

[138] F. C. Flack, E. D. James, and D. M. Schlapp, "Mutual Inductance of Air-Cored Coils: Effect on Design of Radio-Frequency Coupled Implants," *Medical & Biological Engineering*, vol. 9, no. 2, pp. 79-85, Mar. 1971.

[139] K. Fotopoulou and B. W. Flynn, "Wireless Powering of Implanted Sensors Using RF Inductive Coupling," in *5th IEEE Conference on Sensors*, 2006, pp. 765–768.

[140] S. Babic and C. Akyel, "Improvement in Calculation of the Self-and Mutual Inductance of Thin-Wall Solenoids and Disk Coils," *IEEE Transactions on Magnetics*, vol. 36, no. 4, pp. 1970–1975, 2000.

[141] S. I. Babic and C. Akyel, "New Analytic-Numerical Solutions for the Mutual Inductance of Two Coaxial Circular Coils with Rectangular Cross Section in Air," *IEEE Transactions on Magnetics*, vol. 42, no. 6, pp. 1661-1669, 2006.

[142] F. W. Grover, "Tables for the Calculation of the Mutual Inductance of Any Two Coaxial Single-Layer Coils," *Proceedings of the Institute of Radio Engineers*, vol. 21, no. 7, pp. 1039-1049, 1933.

[143] S. I. Babic, C. Akyel, and M. M. Mahmoudi, "Mutual Inductance Calculation between Circular Coils with Lateral and Angular Misalignment," in *Progress in Electromagnetics Research Symposium Proceedings*, Moscow Russia, 2009, vol. 91, pp. 540-544.

[144] Z. Polik, "Examination and Development of RF Inductors by Using the Finite Element Method," B.Sc. Thesis, Széchenyi István University, 2008.

[145] A. C. Polycarpou, *Introduction to the Finite Element Method in Electromagnetics*. Morgan & Claypool Publishers, 2006.

[146] J.-M. Jin, *The Finite Element Method in Electromagnetics*, 2nd ed. New York: Wiley-IEEE Press, 2002.

[147] "COMSOL Multiphysics v3.5 AC/DC Module Model Library." COMSOL AB, 2008.

[148] C. A. Felippa, "Introduction to Finite Element Methods," 2004. [Online]. Available: http://www.colorado.edu/engineering/cas/courses.d/IFEM.d/.

[149] A. C. M. de Queiroz, "Mutual Inductance and Inductance Calculations by Maxwell's Method," *Home page of Dr. Antonio Carlos M. de Queiroz*, 2005. [Online]. Available: http://www.coe.ufrj.br/~acmq/papers/papers.html.

[150] J. Wu, V. Quinn, and G. H. Bernstein, "An Inductive Link with Integrated Receiving Coil—Coupling Coefficient and Link Efficiency," *Journal of Computational Electronics*, vol. 4, no. 3, pp. 221–230, 2005.

# Appendix A

## Ferrite Material Properties

The resistivity and permittivity as a function of frequency are provided in general for MnZn ferrites in [108]:

| Frequency (MHz) | Resistivity (Ωm) | Permittivity ($\varepsilon_r$) |
|---|---|---|
| 0.1 | ≈ 2 | ≈ $2\times10^5$ |
| 1 | ≈ 0.5 | ≈ $10^5$ |
| 10 | ≈ 0.1 | ≈ $5\times10^4$ |
| 100 | ≈ 0.01 | ≈ $10^4$ |

The complex permeability $\mu_r = \mu_r' - j\mu_r''$ is provided specific to the material:

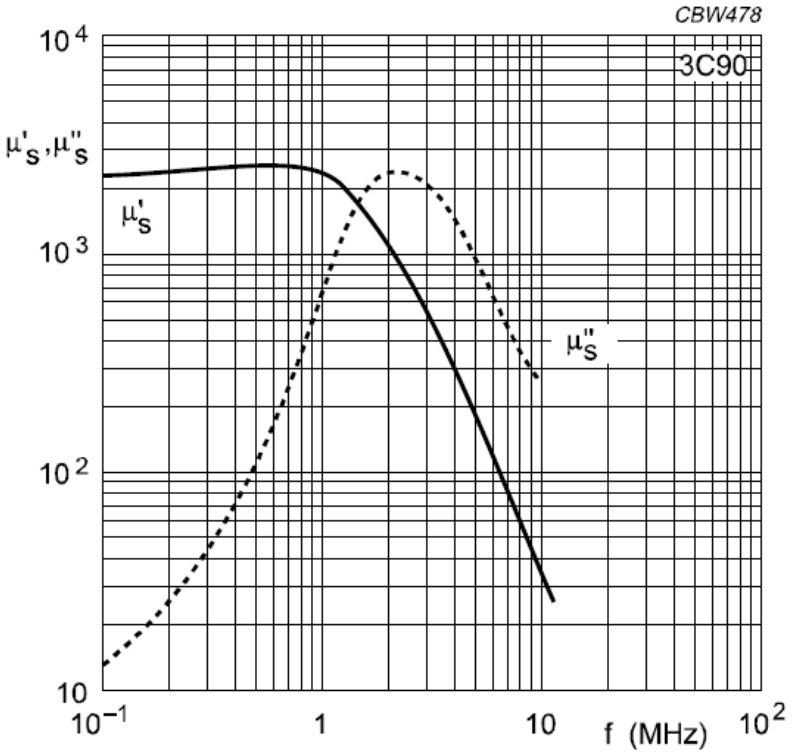


**Figure A.1 Complex permeability as a function of frequency for material 3C90, from [108]**

# Appendix B

## *COMSOL* Settings for 2D Model

Once the coil geometry has been established, the subdomain settings may be specified by selecting Physics > Subdomain Settings (F8), shown in Figure B.1. A different loop voltage variable is specified for each turn. In this particular model, there are 100 turns, a core region, and a surrounding boundary region, resulting in 102 subdomains in total.

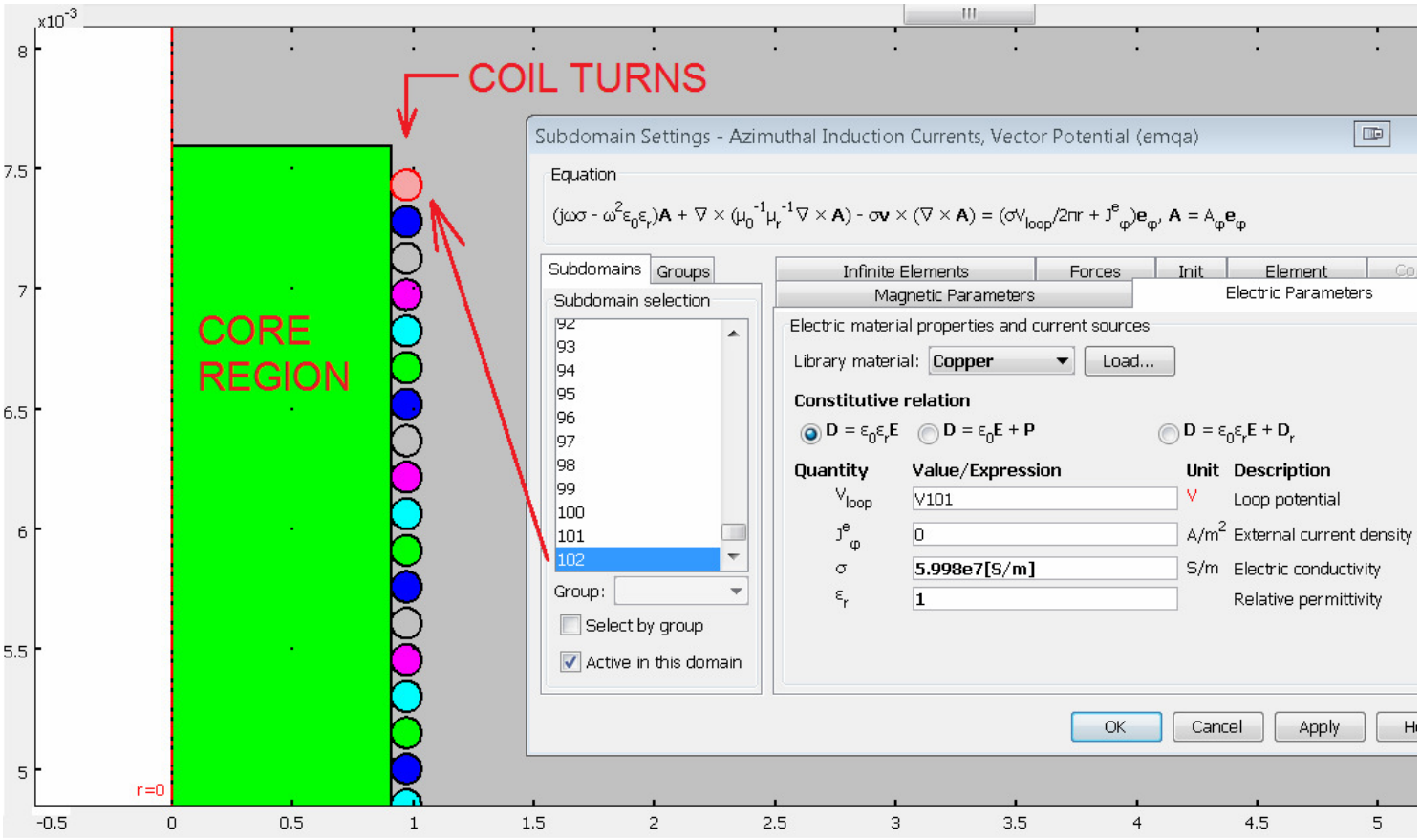


**Figure B.1 Subdomain settings**

The selected subdomain is highlighted by the software in red. The other colours differentiate between different subdomains, but those with the same colour do not necessarily have the same settings. The electrical constants (conductivity and permittivity) are set by defining a material for the subdomains.

The outer boundary subdomain is typically created as a half-circle with a diameter 2 to 3 times larger than the length of the coil. Because the model is axisymmetric this represents a sphere containing the coil. In the subdomain settings dialog box (Figure) this region is set to air, as well as the “infinite element” type of finite element from the Infinite Elements tab. Spherical element type is selected, and default values there are used. This means the model quantities will be calculated as though the enclosing boundary extends (is stretched) to infinity.

Next, the subdomain integration variables are defined from the Options > Integration Coupling Variables > Subdomain Variables dialog box shown in Figure B.2. The current density variable Jphi_emqa is integrated over each subdomain and assigned to a variable name. The default of order 4 was used.

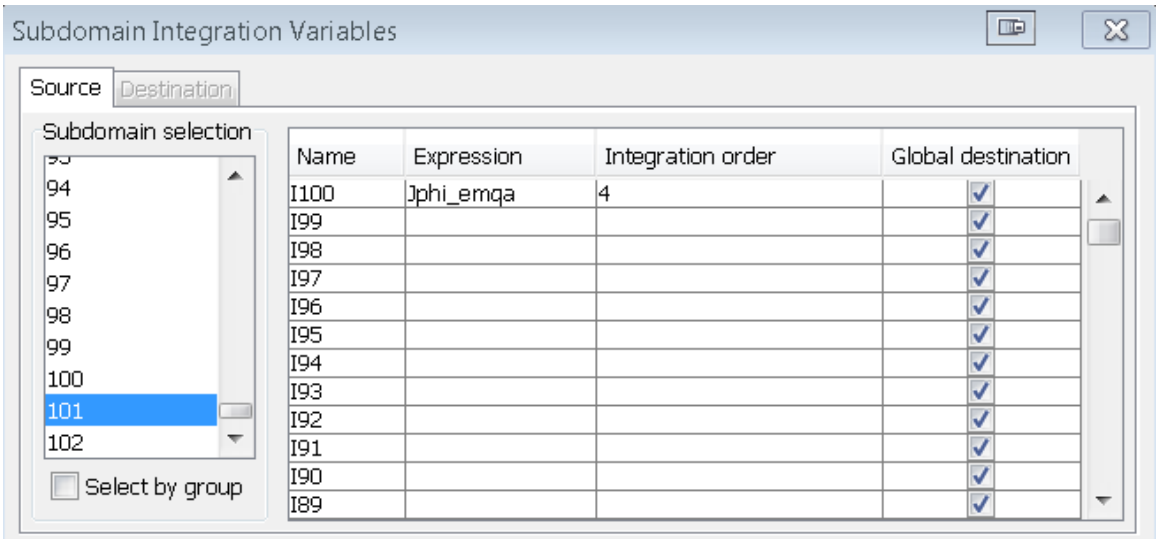


**Figure B.2 Subdomain integration variables**

Once a total coil current has been defined under Options > Constants (see Figure B.3), then a global equation is established for each loop voltage variable as shown in Figure B.4. It was explained in section 6.2 that this causes the loop voltages to vary in order to satisfy the equations when the model is solved. As shown above, the variable names may not necessarily match with the subdomain numbers, but it is helpful if the current variable names correspond to the loop voltage variable names as in Figure B.4.

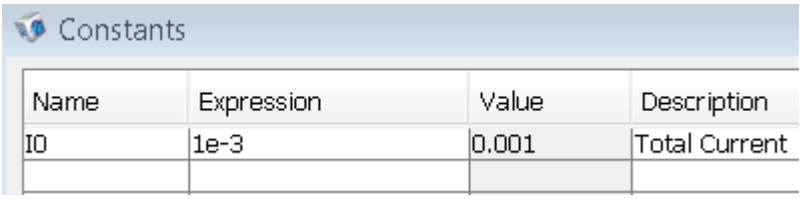


**Figure B.3 Constants definition**

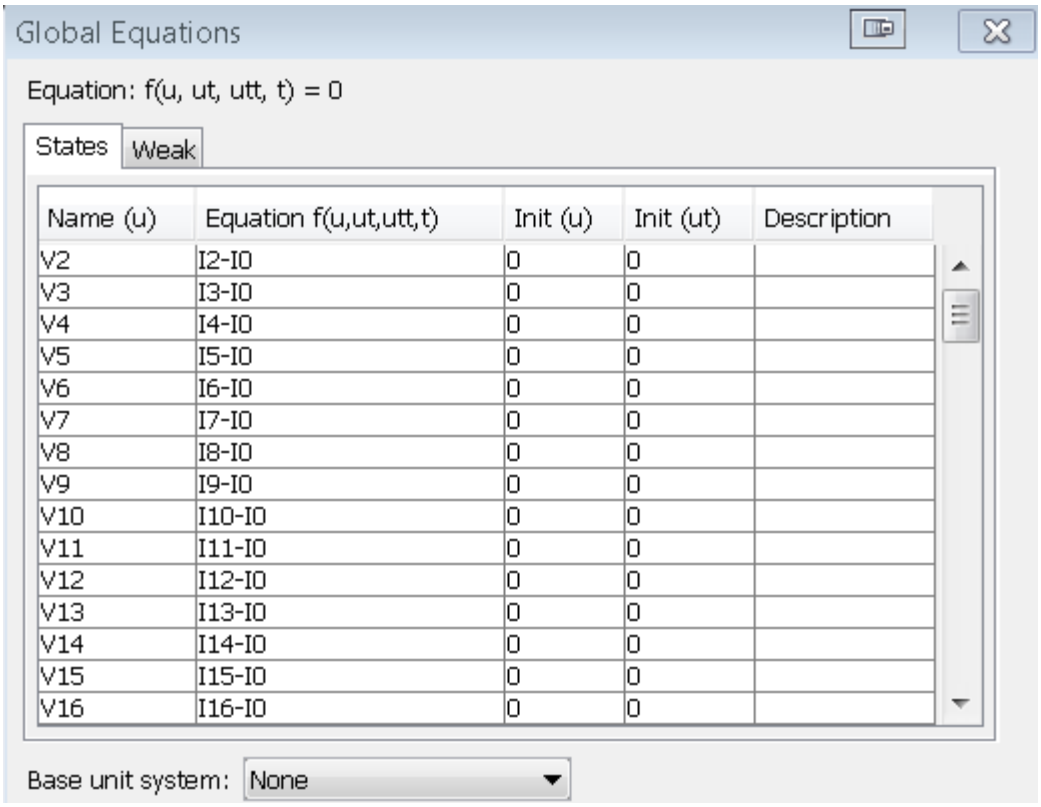


**Figure B.4 Global Equations definition**

Next, the frequency is specified under Physics > Scalar Variables. If this is to be parameterized during the solution, the expression "freq" is entered; otherwise a scalar is input here. It should appear as in Figure B.5 For parameterization, the parameter name "freq" and the list of frequencies is input as parameter values under Solve > Solver Parameters, after selecting parametric on the left of that dialog.

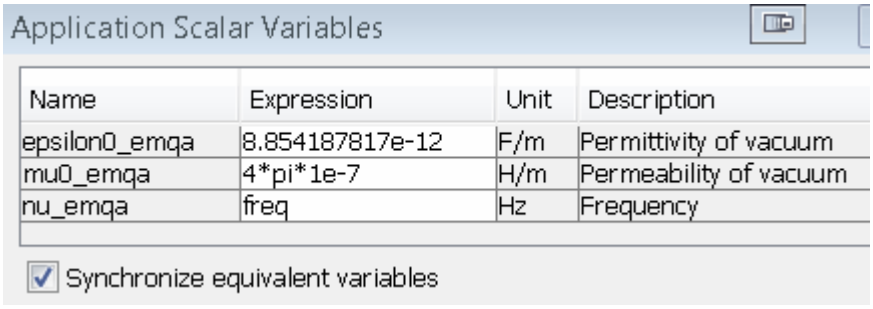


**Figure B.5 Scalar variable definition**

Expressions for the effective resistance and inductance of the coil are defined under Options > Expressions > Scalar Expressions, shown in Figure B.6. As explained in section 6.2, the resistance is obtained from the real part of the impedance, and the inductance from the imaginary part. The full expression for the latter with 100 coil turns is as follows. (The resistance expression uses the 'real' function, and does not have omega in the denominator).

```
imag((V2+V3+V4+V5+V6+V7+V8+V9+V10+V11+V12+V13+V14+V15+V16+V17+V18+V19+
V20+V21+V22+V23+V24+V25+V26+V27+V28+V29+V30+V31+V32+V33+V34+V35+V36+V37
+V38+V39+V40+V41+V42+V43+V44+V45+V46+V47+V48+V49+V50+V51+V52+V53+V54+V5
5+V56+V57+V58+V59+V60+V61+V62+V63+V64+V65+V66+V67+V68+V69+V70+V71+V72+V
73+V74+V75+V76+V77+V78+V79+V80+V81+V82+V83+V84+V85+V86+V87+V88+V89+V90+
V91+V92+V93+V94+V95+V96+V97+V98+V99+V100+V101)/(I0*omega_emqa))
```

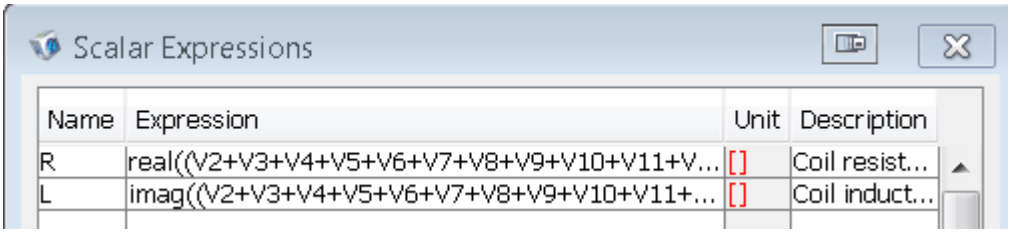


**Figure B.6 Scalar expressions definition**

Finally, these expressions are evaluated after the model has been solved, using Postprocessing > Data Display > Global, and entering ‘R’ or ‘L’ for the expression. The output is displayed at the bottom of the *COMSOL* window.

# Appendix C

## Matlab Script for Helical Coil Geometry

```
%% Fast Henry Input File Generator for Solenoid
clear
clc

%create some output files
fid1 = fopen('fh_large.txt', 'w');
fid2 = fopen('xyzCurve.txt', 'w');

%% Large External Coil
coilRadius = 0.05;
coilLength = 0.1;
wireDiameter = 0.64e-3;
turns = 150;
segmentsPerTurn = 41;

segmentsTotal = turns*segmentsPerTurn;

Zpts = [0:(coilLength/segmentsTotal):coilLength];
Theta = [0:2*pi/segmentsPerTurn:turns*2*pi];
Rho= coilRadius*ones(1,segmentsTotal+1);

[X Y Z] = pol2cart(Theta,Rho,Zpts);
xyzMat = [X' Y' Z'];
plot3(X,Y,Z)

%% FOR COMSOL Line Style "Segment" (start1 end1 start2 end2)
X2 = X(ones(1,2),:);
X2 = X2(:).';
Y2 = Y(ones(1,2),:);
Y2 = Y2(:).';
Z2 = Z(ones(1,2),:);
Z2 = Z2(:).';
xyzMatSegmentStyle = [X2(2:end-1)' Y2(2:end-1)' Z2(2:end-1)'];

%output to screen or txt file using
%fprintf(fileID, format, A, ...)
%% for Fast Henry input
for i = 1:segmentsTotal+1
   fprintf(fid1,'N%d x=%g y=%g z=%g \n',i, xyzMat(i,1),
xyzMat(i,2),xyzMat(i,3));
end

for j = 1:segmentsTotal
   fprintf(fid1,'E%d N%d N%d \n',j, j, j+1);
end
```

# Appendix D

## *COMSOL* Settings for 3D Model

The user interface of *COMSOL* 4 has been improved from that in versions 3. Development of the model proceeds by working downward through the 'Model Builder' tab by right-clicking on the settings there to add objects including geometry, materials, the (governing) physics, the mesh type, the study (solver) type, and finally to do postprocessing including integration or plots.

For the model introduced in section 6.3 specifically, the Magnetic Fields (mf) interface was used, and an Edge Current was defined under it (by right-clicking). This is where the total current applied to the coil is set, after selecting the appropriate edges in the Graphics tab.

The mesh used was Size 'Finer' and type Free Tetrahedral.

In order to perform integration of the magnetic flux when the secondary volume is not parallel with the primary coil, it was necessary to define an additional coordinate system by adding a 'Base Vector System' under Model 1 > Definitions > Coordinate Systems. These new coordinate vectors are specified in terms of the default 'Boundary System 1' vectors (the red-green-blue x-y-z) that appears by default in the Graphics tab for 3D geometry. The new vectors for 30° and 60° axial misalignment were defined as shown in Figure D.1.

The study type selected was frequency domain, and appears under Study1 > Frequency Domain. The list of frequency parameters are input not under 'Step 1' as it may seem, but rather under Solver Configurations > Solver 1 > Stationary Solver 1 >

Parametric. This duplication of places to input the parameters is very counterintuitive for the user, because latter location, as just described is used by the software during solution.

Finally, to perform the integration of the magnetic flux (over the ferrite volume), the following expression is used, which is the dot product of the B-field with the z-axis of the newly defined coordingate system:

```
mf.Bx*sys2.e_z11+mf.By*sys2.e_z12+mf.Bz*sys2.e_z13
```

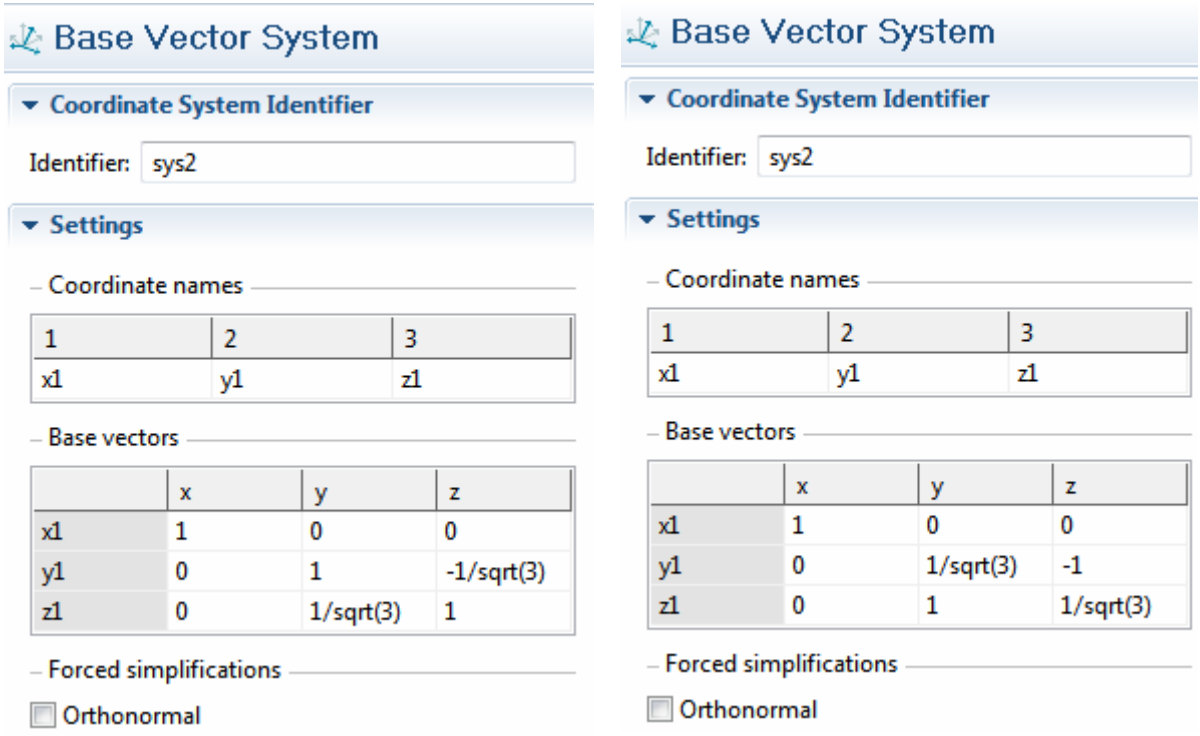


(a) for 30° (b) for 60°

**Figure D.1 Definition of an additional (base vector) coordinate system**

# Appendix E

## Mutual Inductance Calculation from [143] Implemented in *MATLAB (with ferrite factor from* [109]*)*

**Main Script:**

```
%% BABIC & AKYEL 2009 Filament Method
clc;
clear;
%% Physical quantities
mu0 = 4*pi*1e-7; %free-space permeability H·m-1
% ferrite complex permeability (Ferroxcube 3C90)
% using factor DFC from Theilmann & Asbeck
mu1=2510.367586;
mu2=290.3435282;
DFC=3.96E-09;

%% COIL 1 Primary height (2K + 1) by width (2N + 1)
Rp = 0.1/2;  %radius
a  = 0.095; %length (height)
N1 = 14;
hp = 643.8E-06; %thickness
K = 7;
N = 0;

%% COIL 2 Secondary height (2m + 1) by width (2n + 1)
Rs = (0.0015)/2; %radius
b  = 0.010; %length (height)
N2 = 50;
hs = 127E-06; %thickness
m = 50;
n = 0;

%AIR CORE
Mac = 0;
% Matrix for output and graphing
Mmat=zeros(3,3,3);

%VERTICAL Distance between Coil Centres 'Z'
for c = 0: 0.025 :0.05
    % c,d,theta counters to fill Mmat
    c_counter=(c/0.025)+1;
    fprintf ('c = %1.1f \n',c)
    % HORIZONTAL DISTANCE Between Axes at Coil Centre 'R'
    for d = 0:0.02:0.04
        d_counter=(d/0.02)+1;
        fprintf ('  d = %d \n',d)
        %ANGLE Between Axes
        for theta = 0:30:60
```

```
            t_counter=(theta/30)+1;
            fprintf ('   theta = %d \n',theta)

            for g = -K:1:K
                for h = -N:1:N
                    for l = -n:1:n
                        for p = -m:1:m

                            z = c+a.*g./(2.*K+1)-
b.*p.*cosd(theta)./(2.*m+1);
                            Rsl = Rs + hs.*l./(2.*n+1);
                            Rph = Rp + hp.*h./(2.*N+1);
                            dp = d + b.*p.*sind(theta)./(2.*m+1);
                            alpha = Rs./Rph;
                            beta = z./Rph;

                            %use anon function declaration because
integral
                            %requires function of one variable
                            fh = @(phi) babicInteg(theta, phi, dp,
Rsl, Rs, alpha, beta);

                            %numerical integration
                            integ = quad(fh, 0, pi);
                            Mac = Mac +
(mu0./pi)*sqrt(Rph.*Rsl).*integ;
                        end
                    end
                end
            end

            Mac = Mac.*N1.*N2 ./
((2.*K+1).*(2.*N+1).*(2.*m+1).*(2.*n+1));
            %Theilmann & Asbeck DFC factor for complex MU
            M1 = Mac.*mu1./(1+DFC*(mu1-1));
            M2 = Mac.*mu2./(1+DFC*(mu2-1));
            fprintf ('            Mac = %d \n',Mac)
            Mabs = sqrt(M1^2+M2^2);
            fprintf ('            Mabs = %d \n',Mabs)
            Mmat(c_counter, d_counter, t_counter)=Mabs;
        end
    end
end


%Mmat(i,j,k) = Mmat(Z,R,angle)
subplot(3,1,1)
hold
%Z=5
plot([0 2 4],Mmat(3,:,1),'-sb') %0deg
plot([0 2 4],Mmat(3,:,2),'-om') %30deg
plot([0 2 4],Mmat(3,:,3),'-^g') %60deg

title(sprintf('Filamentary Formula\n '),'FontSize',14)
ylabel(sprintf('  \n '),'FontSize',13)
```

```
  legend('0 \circ','30 \circ','60 \circ','Location','NorthEastOutside')
  legend('boxoff','Location','NorthEastOutside')
  set(gca,'FontSize',12)

  subplot(3,1,2)
  hold
  %Z=2.5
  plot([0 2 4],Mmat(2,:,1),'-sb') %0deg
  plot([0 2 4],Mmat(2,:,2),'-om') %30deg
  plot([0 2 4],Mmat(2,:,3),'-^g') %60deg

  %title(sprintf('Z=2.5\n '),'FontSize',14)
  ylabel(sprintf('Magnitude of Mutual Inductance (H) \n
'),'FontSize',13)
  legend('0 \circ','30 \circ','60 \circ','Location','NorthEastOutside')
  legend('hide')
  set(gca,'FontSize',12)

  subplot(3,1,3)
  hold
  %Z=0
  plot([0 2 4],Mmat(1,:,1),'-sb') %0deg
  plot([0 2 4],Mmat(1,:,2),'-om') %30deg
  plot([0 2 4],Mmat(1,:,3),'-^g') %60deg
  xlabel(sprintf(' \n radial distance from coil centre
(cm)'),'FontSize',13)
  %ylabel(sprintf('  \n '),'FontSize',13)
  %title(sprintf('Z=0\n '),'FontSize',14)
  legend('0 \circ','30 \circ','60 \circ','Location','NorthEastOutside')
  legend('hide')
  set(gca,'FontSize',12)
```

**Function G.m:**

```
  function r = G(q)
  %G elliptic integral function used by Soma et Al, Babic et Al
  m=q.^2;
  [K,E] = ellipke(m); %complete elliptic integrals of 1st and 2nd kind
  r= ((2./q)-q).*K-(2./q).*E;
```

**Function BabicInteg.m:**

```
  function ans = babicInteg(theta, phi, dp, Rsl, Rs, alpha, beta)

  xi = beta - alpha.*cos(phi).*sind(theta);
  V = sqrt(1-cos(phi).^2.*sind(theta).^2-
2.*(dp./Rs).*cos(phi).*cosd(theta)+(dp./Rs).^2);
  k = sqrt(4.*alpha.*V./((1+alpha.*V).^2+xi.^2));

  ans = ((cosd(theta)-(dp./Rsl).*cos(phi)).*G(k))./sqrt(V.^3);
```